Visual Hull Method for Realistic 3D Particle Shape Reconstruction Based on High-Resolution Photographs of Snowflakes in Freefall from Multiple Views

***C. Kleinkort, G.-J. Huang, V. N. Bringi, and B. M. Notaroš*†**

Department of Electrical and Computer Engineering

Colorado State University, Fort Collins, CO, USA

Submitted to **Journal of Atmospheric and Oceanic Technology**

9 May 2016

Revised Manuscript, 15 September 2016

Revision 2, 17 December 2016

†Corresponding Author:
Branislav M. Notaroš
Colorado State University
Department of Electrical and Computer Engineering
1373 Campus Delivery
Fort Collins, CO 80523, USA
Phone: (970) 491-3537, Fax: (970) 491-2249
Web: www.engr.colostate.edu/~notaros
E-mail: notaros@colostate.edu

Abstract

A visual hull method for reconstruction of realistic 3D shapes of snowflakes and other hydrometeors based on high-resolution photographs of particles in freefall from multiple views captured by a multi-angle snowflake camera (MASC), or another similar instrument, is proposed and presented. The visual hull of an object is the maximal domain that gives the same silhouettes as the object from a certain set of viewpoints. From the measured fall speed and the particle shape reconstruction, the particle density and dielectric constant are estimated. This is the first time 3D shape reconstructions based on multiple high-resolution photographs of real (measured) snowflakes are performed. The results are clearly much better than any similar data in the literature. They demonstrate – in experiments involved in real snow storm observations and those with simulated and fake 3D printed snowflakes – sufficient silhouette information from the five cameras of the expanded MASC system and excellent performance of the implemented mechanical calibration and software self-calibration of the system. In addition to enabling realistic "particle-by-particle" computations of polarimetric radar measurables for winter precipitation, the visual hull 3D shape reconstructions of hydrometeors can be used for microphysical characteristics analyses, hydrometeor classification, and improvement of radar-based estimations of liquid equivalent snow rates.

1. Introduction

In-situ measurements, remote sensing, and modeling of winter precipitation, which contains a large variability of ice particles, is being heavily investigated to better understand the microphysical characteristics of such particles (e.g., Pruppacher and Klett 2010; Mason 2010). The use of dual-polarized radar observables, horizontal reflectivity, Z_h, differential reflectivity,

Z_{dr}, linear depolarization ratio, LDR, specific differential phase, K_{dp}, and co-polar correlation coefficient, ρ_{hv}, in conjunction with the microphysical properties of ice crystals and aggregates has been demonstrated as a useful and promising approach to classification of winter precipitation (Straka et al. 2000). Conversion of these idealized microphysical characteristics of ice particles into a model that can be used to compute a scattering matrix and in turn radar observables poses great challenges due to the large amount of uncertainty in how accurately the proposed models represent winter precipitation. For instance, the scattering matrix is influenced by the winter particles density, a parameter that can vary substantially based on the type of particle as well as other factors, and when an incorrect density is used, large errors can be introduced (e.g., Matrosov et al. 2009; Zhang et al. 2011). Moreover, idealized spheroidal particle models instead of the more realistic three-dimensional (3D) ones can also result in inaccurate scattering matrix calculations and cause errors in the determination of the snow water equivalent (SWE) (e.g., Du et al. 2010, Tyynelä et al. 2011). Some scattering models with spheroidal shape assumptions for plate or column-like crystals and aggregates have shown consistency with radar measurements when the particle is small compared to the wavelength (e.g., Du et al. 2010, Vivekanandan et al. 1994; Matrosov et al. 2001; Reinking et al. 2002; Kennedy and Rutledge 2011; Andrić et al. 2012).

Kim (2006) showed that the use of spheroid approximations is only valid for smaller particles; as the snowflakes become electrically larger, the shape properties of the particles start to play a large role in scattering calculations. Ishimoto (2008) performed the finite-difference time-domain scattering calculations of the backscattering cross-sections of ice particles using fractal based snowflake models. These results showed large differences between equivalent-volume spheres and hexagonal columns, giving rise to the need for more accurate snowflake models. Furthermore, the evaluation of the sensitivity of snowfall characteristics at high frequencies, using idealized simulated snowflake models, indicated a need for a scattering database for large particles and aggregates as their shapes vary immensely and play a large role in determining snowfall characteristics (Kneifel et al. 2010). Kim et al. (2007) created idealized ice crystal models in the form of hexagonal columns, four-arm rosettes, and six-arm rosettes, and used the discrete dipole approximation (DDA) method to calculate scattering effects of these geometries. Multiple other papers present the use of the DDA method to compute single-scattering properties of synthetic randomly oriented idealized simple ice crystals. The results show that the scattering parameters of these idealized snowflakes are highly sensitive to shape and electrical size, again leading to the need for accurate and realistic models (Hong 2007a, Liu 2010, Evans et al. 1995, Kim et al. 2007, Hong 2007b, and Grecu and Olson 2008). In addition, notable previous studies of the ice scattering problems are those by Yang et al. (2005; 2013), Liu (2008), and Petty and Huang (2010), among others.

Kuo et al. (2016) use the DDA method to compute the single-scattering properties of individual synthetic snowflakes, where each snowflake is simulated and averaged over 900 different directions. These synthetic 3D snowflakes are created by a random aggregation, based on a sophisticated collection algorithm, of different pristine ice crystal models. The created synthetic 3D models of aggregates have mass-versus-size and fractal properties that are consistent with field observations. A main conclusion of this work is that spherical particle models cannot be used to simulate single-scattering properties in a way that is consistent with the nonspherical snow particles of the same mass, across a very large frequency range, 10 GHz to 183 GHz (Kuo et al. 2016). The discrepancies shown between complex snowflake models and spherical representations in this work give rise to the need for complex 3D models that accurately represent the snow that is falling at any given time.

However, even when Rayleigh scattering is considered, while it may provide reasonable results for the computation of reflectivity Z_e (Ryzhkov et al. 1998), an assumption of spheroidal shape is not sufficient to accurately compute the full scattering matrix and the dual-polarization radar measurables such as Z_{dr}, LDR, and ρ_{hv}. So even at the S-band (all WSR-88D radars), these radar measurables, which play an integral role in radar-based particle classification schemes, are highly shape dependent; this once more leads to the need for better and more realistic models of the winter precipitation particles.

Indeed, better and more realistic models of the winter precipitation particles can be obtained based on observations using advanced optical imaging disdrometers, which can record and measure actual geometrical shape, size, and composition properties of natural snowflakes and other hydrometeors in freefall. The 2D-video disdrometer (2DVD) measures fall speed along with projected hydrometeor views in two planes, namely, it gives two mutually orthogonal contour images of the particle, using high-speed line-scan cameras (Barthazy et al. 2004). The multi-angle snowflake camera (MASC) captures high-resolution photographs of snowflakes and other ice particles in freefall from three views, while simultaneously measuring fall speed (Garrett et al. 2012). Teschl et al. (2006) used the 2DVD to create reconstructions of a snowflake based on two orthogonal views. The two orthogonal contours obtained from the 2DVD are intersected with a sphere that just encases the recorded particle, and parts of the sphere that do not intersect with the contours are deleted. Huang et al. (2014) use a similar method of creating reconstructions of particles imaged by a 2DVD by modeling the particle as an ellipsoid that just encloses the boundaries of the two orthogonal views obtained from the 2DVD. Work by Garret et al. (2012) has involved creating a separate 3D reconstruction of a snowflake for each individual MASC image by extruding the 2D silhouette of the image until an equivalent volume, based on an equivalent radius determined from the image, is reached.

This paper focuses on in-situ measurements of hydrometeor shape, size, and composition using advanced optical instrumentation and methods, techniques of image and computational analysis, and processing of these measured characteristics to arrive at geometrical, physical, and scattering models of natural snow and ice particles. These models can further be processed and analyzed to compute realistic particle scattering matrices and full polarimetric radar measurables, namely, Z_h, Z_dr, LDR, K_dp, and ρ_hv, to analyze microphysical characteristics of particles, perform studies of snow habits, and develop and use classifications of hydrometeor types. The paper proposes and presents a visual hull method and technique for reconstruction of realistic 3D shapes of snowflakes and other hydrometeors based on high-resolution photographs of particles in freefall from multiple views captured by a multi-angle snowflake camera. The visual hull of an object can be interpreted as the maximal domain that gives the same silhouettes as the object from a certain set of viewpoints. The 3D reconstructed snowflakes are represented by fine surface meshes of flat triangular patches, which capture a large amount of detail about the shape of the free-falling snowflakes. In order to improve the 3D reconstructions obtained from the visual hull method, two extra cameras are added to the three original cameras of the MASC, "externally," to provide additional 3D spatial information about the hydrometeor's shape. We carry out an improved mechanical calibration procedure of the MASC system involving all cameras of the system together. Furthermore, we perform a five-camera software self-calibration of the MASC, to obtain a matrix describing the cameras internal and external parameters, which is then used as an input to the visual hull code to correct for a non-perfect mechanical calibration, a crucial step for the accuracy and reliability of shape reconstructions based on the MASC photographs. We use the fall speed measured by the MASC and the horizontal cross-sectional projected area of the visual hull 3D reconstruction of the particle, along with state parameters measured at the MASC site, to estimate the particle mass, according to Böhm's method (Böhm 1989). From the mass and volume of the meshed particle, we estimate the density, and then the dielectric constant of each snowflake, based on a Maxwell-Garnet formula (Maxwell-Garnet 1904). These scattering models of snow and ice particles can be used for computation of particle scattering matrices and full dual-polarized radar observables; for instance, this can be done using a computational electromagnetic technique based on the higher order method of moments (MoM) in the surface integral equation (SIE) formulation (Chobanyan et al. 2015). To be able to perform scattering analysis by the MoM-SIE scattering code (Chobanyan et al. 2015), we convert the visual hull generated triangular mesh to a mesh with curved generalized quadrilateral patches. In addition, from these triangular patch meshes, representing realistic complex 3D shapes of snow and ice particles, we are also able to compute the volume, surface area, shape characteristics, and spatial complexity of the hydrometeor, all extremely useful for various microphysical characterizations of winter precipitation.

Note that the effects of modeling the particle's interior as a homogeneous dielectric need to be quantified further. Using homogeneous interior of a particle and the Maxwell-Garnet model is valid at low frequencies such as S- to X-bands. However, more work will need to be done in the future to determine how to more accurately model the interior of the snowflake relevant for scattering at higher frequencies such as Ka- and W-bands. Leinonen et al. (2013) simulated snow aggregation using Westbrook et al. (2006) and Westbrook (2008) models and found that the mass distribution in an aggregated snowflake is closed to Gaussian. This nonuniform distribution can affect higher-frequency (above Ku-band) radar measurements. More recent study of Leinonen and Szyrmer (2015) compared the true backscattering cross section (using the DDA method) at Ku, Ka, and W-bands with a spheroidal model (in conjunction with the T-matrix method) for the simulated snowflake. The results showed that nonuniform mass distribution will cause model scattering saturated at smaller size.

The rest of the paper is organized as follows. Section 2 presents the MASC and the modified five-camera MASC system, as well as the in-situ instrumentation site providing the context of the study. Section 3 discusses the proposed visual hull method for 3D shape reconstruction of snowflakes from multiple images. In Section 4, we explain mechanical calibration and software self-calibration of the five-camera MASC system. Section 5 describes meshing, dielectric constant estimation, scattering analysis, and automatization of the process. In Section 6, the proposed visual hull method for 3D hydrometeor shape reconstruction is validated, evaluated, and discussed in a number of characteristic examples. Section 7 provides concluding remarks.

2. Multi-Angle Snowflake Camera, Modified MASC System, MASCRAD Instrumentation Site

The context of the proposed and presented visual hull method for reconstruction of 3D shapes of snowflakes and other hydrometeors is constituted by remote sensing observations and surface measurements, followed by analysis, of winter precipitation at an in-situ instrumentation site such as the newly built and established surface instrumentation field site for the MASCRAD (MASC + Radar) project (Notaros et al. 2015a, Notaros et al. 2015b, Kenedy et al. 2015, Bringi et al. 2015, Notaroš et al. 2016). The MASCRAD Field Site, shown in Figure 1, at the Easton

Valley View Airport, in La Salle, near Greeley, Colorado, includes a double wind fence housing a multi-angle snowflake camera (MASC) and several other advanced instruments, under the umbrella of the state-of-the-art polarimetric weather radar, CSU-CHILL S-Band (2.725 GHz) Radar, with the instrumentation site being very conveniently located at a range of 12.92 km from the radar (Notaroš et al. 2016).

At the heart of the MASCRAD project is the MASC, shown in Figure 2, which is a new instrument for capturing high-resolution photographs of snowflakes in freefall from three views, while simultaneously measuring their fall speed (Garrett et al. 2012). For Colorado State University's customized system, the horizontal resolution is 35 μm for all three cameras and the vertical resolution at 1-m/s fall speed is 40 μm, and the virtual measurement area is 30 cm^2. It has three identical cameras, 5 Megapixel (MP) Unibrain Fire-i 980b digital cameras, with identical lenses, Fujinon 12.5 mm. In a MASC, the angular separation in the horizontal plane between each of the two adjacent cameras is 36° and the camera-to-common focal center distance is 10 cm. Particles that fall through the lower near-IR emitter-detector pair array simultaneously trigger each of the three cameras and the bank of LEDs. In addition to taking pictures, at a maximum triggering rate of 2 Hz, the fall speed of a particle is calculated from the time taken to traverse the distance between the upper and lower triggering arrays, which are separated vertically by 32 mm. In order to improve the 3D reconstruction obtained from the visual hull method, two additional lower-resolution cameras (1.2 MP Unibrain Fire-i 785b cameras, with 12.5-mm lenses) were added to the MASC, "externally" on an elevated plane with respect to the original three MASC cameras, as shown in Figure 2, to provide additional views – this will be discussed in detail later in the paper. Figure 3 shows three examples of MASC snowflake five-image sets collected at the MASCRAD Field Site.

3. Visual Hull Method for 3D Shape Reconstruction of Snowflakes from Multiple Images

3D reconstruction is a popular subject in computer vision (Hartley and Zisserman, 2000) and can be applied to many areas such as medical visualization, virtual reality, multimedia, and so on. One of the most straightforward approaches to shape reconstruction is based on the visual hull method, which uses serial calibrated silhouettes obtained from multiple view angles surrounding the target to recreate its 3D shape (Laurentini 1994; 1995; Baumgart 1974; Matusik et al. 2000; Forbes 2007). We propose the use of the visual hull geometrical method to reconstruct 3D shapes of hydrometeors based on the sets of five (or a different number) photographs obtained by the MASC (see Figures 1–3), or another similar instrument, and the corresponding 2D silhouettes of an object (Kleinkort et al. 2015a; 2015b). This enables the computation of "particle-by-particle" scattering matrices, and can as well be used for studies of snow habits, for advanced analyses of microphysical characteristics of particles, and for particle classifications. The visual hull of an object can be interpreted as the maximal domain, or largest volume, that gives the same silhouettes as the object when viewed from a certain set of viewpoints (theoretically, from any viewpoint) (Laurentini 1994). Visual solid cones are formed by back-projecting, from the set of viewpoints, the previously found silhouettes in the corresponding image planes situated in front of the cameras, and the visual hull is obtained as an intersection of such cones. This is illustrated in Figure 4. The visual cone of each silhouette refers to the projected volume of space extending from the camera's lens that the observed object lies completely inside. A limitation of the visual hull method is the inability to capture concave features due to these features not affecting the silhouette obtained from each image. This leads to the perfectly calibrated visual hull always being an overestimate of the object's volume as will be shown in the calibration section. In specific, we use an open-source MATLAB, C++ Visual Hull Mesh Code (VHMC 2012), which generates a visual-hull mesh from silhouette images of an object and associated camera parameters, created initially for identifying stones based on certain shape parameters obtained from 3D reconstructions. We have modified this code to work for our purpose of reconstructing snowflakes which are of a much smaller size scale.

The intersection of the visual solid cones creates a surface that reconstructs the hydrometeor's geometry. Each visual solid cone creates at least one closed surface region on the exterior of the hydrometeor's geometry; more than one surface region per visual cone is created if there are holes, or air gaps, present in the hydrometeor's silhouette. Points where the surface regions have a width of zero are called frontier points and are intersections of two or more visual solid cones. Frontier points lie directly on the actual hydrometeor's surface and regions near these frontier points are very accurately reconstructed. It is desired to have frontier points well distributed over a sphere in order to accurately reconstruct arbitrary shapes. As will be shown in a later section, the positions of the original three cameras in the MASC did not create representative reconstructions of snowflakes so two additional cameras were added (Figure 2) to aid in the even distribution of these frontier points.

Before the visual hull code can be run on a set of five (or three) images, a number of preprocessing steps must be taken to ensure quality 3D reconstructions. In order to determine what is part of the background and what is part of the foreground, a mean and standard deviation of the background for all five (three) cameras is calculated over an hour period that corresponds to the image set being processed. The calculated mean and standard deviation are given as follows:

$$\overline{im} = \frac{1}{N}\sum_{i=1}^{N} im_i$$
$$STD(im) = \frac{1}{N-1}\sum_{i=1}^{N}(im_i - \overline{im})^2$$

where *im* corresponds to the matrix that describes a gray scale image, $\overline{im}$ is the mean, *STD* is the standard deviation, im_i is the matrix of the i^{th} image in term of intensity (0-255) of image, and N is the number of pictures for each camera within the hour of calculation.

These calculated background values are used to subtract the backgrounds from the five images being processed to account for any variations in lighting conditions, changes in the background, the visible infrared bulbs, and all other variations that might occur from hour to hour and be mistaken as part of the foreground. Figure 5 shows an example of the mean and standard deviation calculated for use in background removal from MASC images. The IR bulbs used in sensing snowflakes can be seen by two of the five cameras (Figure 5, Cam3 and Cam 5) and appear as white dots in the image that visual hull will mistake for snowflakes. During daytime observations, the ground and DFIR fence slats (Figure 1) can be seen in the images. The background removal technique removes these bright spots, the fence slats, as well as other variations that might be mistaken for hydrometeors and allows for high quality reconstructions of snowflakes from the visual hull method. With the implementation of image processing techniques, lighting conditions that vary throughout the day and night have no effect on whether or not reconstructions of hydrometeors can be made.

The majority of the images collected by the MASC contain more than one snowflake per image, as shown in Figure 6. Before these images can be processed by the visual hull method, the snowflakes need to be counted, separated, and matched. If the images are input into visual hull without any pre-processing, the visual hull code will fail to create reconstructions for every snowflake. To do this, an image processing code has been created that boxes and counts the individual snowflakes present in each of the five images. Sobel edge detection method (Sobel 1970) are used to find where the snowflakes start and background ends and a box is placed around each individual snowflake, as depicted in Figure 7. Each camera's field of view (FOV) does not perfectly overlap, so the number of snowflakes imaged by each camera may be different. For the visual hull method to successfully create a 3D reconstruction, the snowflake must be present in each of the five camera's FOV. After the snowflakes have been boxed, the number in each image is counted and the image with the least number of snowflakes present is selected as the "starting image" for visual hull. In Figure 7, the image that contains the least number of snowflakes is seen by Camera 5 and contains 3 snowflakes and is called the starting image. This starting image is divided into individual images where each image only contains one snowflake, while the other snowflakes are blacked out and removed (Figure 8). Each of these images that contain only one snowflake, three in this example, are run through visual hull with the remaining four images. It is not necessary to separate the four remaining images into individual flake images as the visual hull code will only search for a point that can be projected back to all five images. If a point on the starting image can be found that corresponds with a point on the remaining four images, a match is found and a reconstruction can be created for this particle. If these three snowflakes are present in the FOV of the other 4 cameras, a 3D reconstruction will be created for each of them.

Along with the five images input to the visual hull code, many parameters that define the camera properties and positions must also be defined and input to the code. These parameters include the camera rotation and translation in 3D space, called the extrinsic parameters, and the focal point, principal points, and distortion, called the intrinsic parameters. A self-calibration code described in the following section gives a way to accurately compute these extrinsic and intrinsic parameters. Other parameters given as inputs to the visual hull code include the resolution of each camera and the size of each camera's charge-coupled device (CCD). For the CSU MASC (Figure 2), the original three "internal" cameras have a 5 MP resolution, 2448 x 2048 pixels, a 12.5 mm focal point, a 2/3" CCD sensor, and a working distance (the distance at which the cameras are focused) of 10 cm. The additional two "external" cameras have a 1.2 MP resolution, 1288 x 964 pixels, a 12.5 mm focal point, a 1/3" CCD sensor, and a working distance of 16 cm.

After background removal process, multiple-snowflake image preprocessing, and specification and input of all camera parameters, the working volume, i.e., the volume intersection of all five camera's FOVs, is discretized into voxels of a desired size to adequately represent the hydrometeor's geometry. The five images are transformed into silhouettes made up of polygons of a desired size. The visual hull code then randomly searches for a center point of a voxel that can be projected to each of the five camera's silhouettes that represents the snowflake within each of the images. Once a point is found, the code starts to build a voxel grid around the projected point until no more voxel center points can be projected to all five cameras. These voxels are then polygonised into a triangular surface mesh using the method developed by Bloomenthal (1994). After the 3D surface reconstruction of the hydrometeor is generated, it is re-projected onto the 2D images as green silhouettes to check how well the geometry matches and represents the 2D images. An example of the 3D reconstruction from a set of five MASC photographs and the 2D re-projection of the reconstructed shape onto the original five images is shown in Figure 9. The size of the voxel grid and triangular mesh patch can be set to capture the desired amount of details and fine features, as depicted in Figure 10.

As can be seen in Figure 10, changing the voxel size in visual hull changes the volume, surface area, shape and aspect ratio of the snowflake. To determine the aspect ratio, the smallest ellipsoid that encloses the particle is computed. From this ellipsoid the aspect ratio is computed as the average of the two minor axes is divided by the major axis. The Decreasing the voxel size leads to a more accurate representation of the snowflake at the expense of more computational time. To determine what voxel size should be used, a random set of snowflakes was reconstructed multiple times with a decreasing voxel size. The percent change after each refinement of the reconstruction's volume, surface area, and aspect ratio are plotted in Figure 11. The level of refinement number corresponds to the number of divisions along one side of a box that bounds the working volume of the five cameras. After a level of refinement of 500 divisions along the bounding box's edge, the change in volume, surface area, and aspect ratio is less than 5%, and for this reason a level of refinement of 500 is adopted as a general parameter in the method for all further reconstructions.

The final 3D model is represented by a mesh of flat triangular patches. These triangular patch meshes, representing realistic complex 3D shapes of snow and ice particles, are used for scattering computations by means of the method of moments computational electromagnetics code, to obtain "particle-by-particle" scattering matrices and polarimetric radar observables. In addition, from these meshes, we are also able to compute the volume, surface area, shape characteristics, and spatial complexity of the hydrometeor, all extremely useful for various microphysical characterizations of winter precipitation.

As shown in Figure 2, the original MASC is a 3 camera system where all of the cameras are coplanar and separated by 36° with respect to each other in the azimuthal direction, covering only 72° in front of the object. The visual hull method works best when cameras are well distributed over a sphere and focused at the sphere's center (Forbes 2007). When looking at a large number of reconstructions generated when only using three coplanar cameras, the 3D reconstructed snowflakes from the three MASC photographs are, generally, not close enough to the real shapes of the hydrometeors. For this reason, two additional cameras were added to the MASC externally on an elevated plane, 55° with respect to the horizon and 72° away from the outer original cameras. The positions of these additional cameras were chosen based on two main requirements: obtaining the most new information, i.e., new azimuthal angles and a different elevation plane; and the mechanical constraints of placing the cameras keeping in mind where the light sources are.

Table 1 gives the azimuthal and elevation positions of all five cameras in the new MASC system.

4. Mechanical Calibration and Software Self-Calibration of the Five-Camera MASC System

The visual hull 3D reconstruction method assumes that the camera system is perfectly calibrated, meaning that the intrinsic and extrinsic parameters of the system are perfectly known. The extrinsic parameters refer to the rotation matrix, R^i and translation matrix, t^i for each of the five camera positions, and to the positions and orientations of the five cameras in physical space. The intrinsic parameters of the cameras refer to the focal length, principal points, and distortion, and are dependent on the camera body and lens.

These extrinsic and intrinsic parameters were initially estimated and input into the visual hull code. The estimation of the extrinsic parameters was based on the theoretical camera positions as determined by the manufacturer of the device. The intrinsic parameters were estimated using theoretical equations that relate them to the camera and lens parameters as follows:

$$M_{res} = \frac{FOV}{R}, \qquad M_{res} = \frac{P_s * FOV}{d_f}, \qquad R = \frac{d_f}{P_s}$$

$$FOV = 2 * d_s * \tan\left(\frac{AOV}{2}\right), \qquad AOV = 2 * \arctan(\frac{d_f}{2 * f})$$

$$R = \frac{1000 * 10^{-6}}{2 * P_p}\ , \qquad d_f = P_p * R$$

with description of variables given in Table 2.

These estimations may be acceptable for 3D reconstructions of larger objects such as fruits, rocks or people; however, for the size scale of snowflakes, a much more accurate estimation, on the order of a few pixels, is needed for these intrinsic and extrinsic parameters. The 3D reconstructions of snowflakes created using formula estimated intrinsic and extrinsic parameters are not representative of the actual snowflakes geometry. Reconstructions are rarely able to be created when these estimation of camera parameters are used. When projecting the 3D reconstruction, if it is able to be created, as silhouettes onto the original image set, the coverage of the re-projection is very poor and much of the snowflakes geometry is cut off and ignored. To fix these mismatches and poor reconstructions, mechanical and software calibrations of the camera system were implemented.

The mechanical calibration procedure involves positioning the five cameras in such a way that they are focused on a single point as close as possible. To do this, instead of a standard procedure of using a target grid that is moved between all of the five cameras separately, one calibration grid is placed in the center of the observational area tilted at a 30° azimuthal angle, from the horizon, so that it is completely visible to all five cameras simultaneously. We use a 5 x 5 calibration grid, with crosshairs in the center grid, created with known black and white box sizes of 5 mm. The cameras are then individually run in a video mode so their image can be seen in real time on a computer screen. Using MB-Ruler (Bader), a reference grid is overlaid on the computer screen with crosshairs at the center of the screen. For each camera, the camera mount is mechanically adjusted, as precisely as possible, to overlap the physical crosshairs on the calibration grid with the crosshairs on the computer screen, as shown in Figure 12. The focal point of the camera is then adjusted to be as close to the center of the crosshairs as possible. The mechanical calibration allows for the depth of field (DOF) of all cameras to overlap as much as possible, which leads to a greater number of image sets where all 5 images are in good focus. Another parameter that is experimentally calculated based on the grid used in the mechanical calibration is the horizontal and vertical field of view (FOV) of the cameras. After mechanical calibration is complete, a new test to characterize the DOF and its relationship with the size of the particle was implemented based on previous work related to the snowflake video imager (SVI) (Newman et al. 2009). The DOF along with the FOV are very important parameters used to calculate the observed volume, which is needed when calculating the particle size distribution of snowflakes from the individual cameras.

However, even with this mechanical calibration procedure implemented, the visual hull reconstructions still miss parts of the snowflakes geometry, as shown in Figure 13. A software calibration was implemented to adjust for this imperfect mechanical calibration. Namely, an open source multi-camera software self-calibration is utilized with modifications to accurately estimate the internal and external parameters of each camera (Svoboda et al. 2005), which, in turn, are used to calculate the position matrix, needed as an input for visual hull. The main functionality and implementation of the self-calibration algorithm is laid out below.

The input to the self-calibration code is a collection of "point images" that adequately fill up the working volume of the cameras, i.e., the volume that is visualized by all five cameras simultaneously. A thin bamboo stick that is painted black with a small white tip is moved around the working volume while the cameras are manually triggered. The projections of these points in each of the 2D images are initially detected by first computing the mean and standard deviation of the background and comparing the actual image to these computed background images. If the detected point is much larger than expected, if the pixels of the detected point are not connected, or if the detected point contains motion blur based on the eccentricity of the point, the image is discarded and is considered a mis-detected point. The detected points are resampled to obtain higher resolution and then a 2D Gaussian function is fit to the point to determine its position. Constraints based on epipolar geometry, in the form of geometric relations between 3D points and their 2D projections based on 2 cameras, further remove any mis-detected points. A random sample consensus (RANSAC; Fischler and Bolles 1981) method is used to iteratively determine epipolar geometry of camera pairs and removes any points that do not fit within the epipolar constraints of the cameras. A scaled measurement matrix W_s is constructed as (Svoboda et al. 2005)

$$W_s = \lambda_j^i \begin{bmatrix} u_j^i \\ v_j^i \\ 1 \end{bmatrix} = \lambda_j^i \boldsymbol{u}_j^{\boldsymbol{i}} = P^{\boldsymbol{i}} \boldsymbol{X}_j$$

where $\boldsymbol{X}_j$ is the projective shape matrix that represents the 3D coordinates of the *j* detected points, $\boldsymbol{u}_j^{\boldsymbol{i}}$ are the pixel *u*-*v* coordinates, u_j^i and v_j^i, of the 2D projected *j* points for camera *i*, λ_j^i is the projective depth for the j^{th} point on the i^{th} camera, and $P^{\boldsymbol{i}}$ is the projective motion matrix for the i^{th} camera that contains the cameras' position, internal parameters, and external parameters. In this equation, the only known variable is $\boldsymbol{u}_{\boldsymbol{j}}^{\boldsymbol{i}}$ which is obtained from a set of knowns points (white tip of a bamboo stick in our case) in the pictures. The variables being estimated in the self-calibration code are the projective depths λ_j^i and the projection matrices $P^{\boldsymbol{i}}$. The Sturm and Triggs method (1996) is used to estimate the projective depth and obtain $\boldsymbol{W}_s$. Even with $\boldsymbol{W_s}$ determined, the solution of the equation is not unique due to the following:

$$\boldsymbol{W_s} = P^i\boldsymbol{X_j} = P^i\boldsymbol{H}\boldsymbol{H}^{-\boldsymbol{1}}\boldsymbol{X_j} = \hat{P}^i\widehat{\boldsymbol{X}}_{\boldsymbol{j}}$$

where $\boldsymbol{H}$ is any nonsingular matrix so that $\boldsymbol{H}\boldsymbol{H}^{-\boldsymbol{1}}$ is an identity matrix, $\hat{P}^i = P^i\boldsymbol{H}$, and $\widehat{\boldsymbol{X}}_{\boldsymbol{j}} = \boldsymbol{H}^{-\boldsymbol{1}}\boldsymbol{X_j}$. The self-calibration code uses Euclidean stratification (Hartley and Zisserman 2000) to obtain an appropriate H so that $\hat{X}_j$ re-projecting to each camera has a minimum least-square error. Once the projection matrices are known they can be decomposed into an internal and external parameter matrix, and a position matrix that is needed as an input to the visual hull code.

This corrected position matrix is input into the visual hull code and is used to correct for the non-perfect mechanical calibration. After both mechanical and software self-calibration have been implemented, the projections of the 3D reconstructed geometries as silhouettes onto the original snowflake images show over 90% coverage in all cases, as can be seen in the results section.

5. Meshing, Dielectric Constant Estimation, Scattering Analysis, and Automatization of Process

Our scattering models of snow and ice particles and realistic computation of scattering matrices and full polarimetric radar observables for precipitation particles are based primarily on the higher order method of moments (MoM) in conjunction with the surface integral equation (SIE) formulation (Chobanyan et al. 2015, Notaroš et al. 2015c, and Djordjević and Notaroš 2004). In this technique, the surface of a dielectric scatterer (precipitation particle) is modeled using generalized curved quadrilateral patches. A method based on ANSYS ICEM CFD meshing software (ANSYS ICEM CFD, 2014) has been created to convert the VHMC-generated mesh of flat triangular patches to a curvilinear quadrilateral mesh. A TCL script was written to perform and automate multiple meshing steps within ANSYS all the way from file import to exporting a good quality quadrilateral mesh, with no user input. First the STL (stereolithography) file obtained from the visual hull code is imported as a solid geometry instead of a triangular mesh. Then the geometry is checked for errors and a watertight volume is created. The snowflake size is evaluated, and based on that, meshing parameters are specified so that the number of elements in the mesh is as needed for an adequate representation of the geometry. The mesh is checked for intersecting elements, negative determinants, size uniformity, and angles of connecting elements, as well as other parameters needed for a good quality mesh. Note that such mesh checks and improvements would be needed even if a scattering code based on a mesh of flat triangular patches as input were used. Figure 14 shows examples of 3D shape reconstruction of real snow particles using the VHMC code and ANSYS ICEM CFD meshing software.

From the triangular patch meshes (e.g., in Figure 9), we are able to compute readily, within the visual hull code, the volume of the 3D reconstructed particle, and thus obtain the volume estimation for the hydrometeor, which is needed for the estimation of the dielectric constant. Furthermore, we are able to obtain, from the 3D particle reconstruction, the horizontal cross sectional drag information, i.e., the particle's projected area presented to the flow, used, in Böhm's method (Böhm 1989), in conjunction with the recorded fall-speed of the particle and environmental conditions such as air density, viscosity, and temperature measured at the MASC site, to estimate the particle's mass. We do this similarly to the approach described in Huang et al. (2015). From the mass and volume, we find the effective density or porosity of the particle (snowflake), from which, in turn, we are able to obtain its effective dielectric constant, ε_r, based on a Maxwell-Garnet formula. Such ε_r takes into account air inclusions and partly melted regions of ice crystals, apart from some of the porosity of the ice particle captured by the MASC/visual hull, along with its complex shape.

Scattering analysis of the 3D reconstructed snowflakes, with the estimated dielectric constants, is carried out on a particle-by-particle basis using the MoM-SIE method. The outcome of the computation are polarimetric radar measurables (Z_h, Z_{dr}, LDR, K_{dp}, and ρ_{hv}), which are then analyzed and compared against the respective measurements by the CSU-CHILL radar.

Due to the large quantity of data we have collected, e.g., approximately 500,000 snowflakes captured and recorded at the MASCRAD Field Site (in Figure 1) during the 2014/2015 winter season, the data processing must be completely automatic from the collection of the image sets to the generation of the radar observables. To do this, a MATLAB control code was created that connects and automates all of the individual processes. The only user input is determining which snowflakes to process, in terms of snowflake IDs, a parameter defined during MASC image capture, or a time range. Once the range is specified, the image processing code that boxes, counts, and separates snowflakes is run. The output of this code is used as an input to the visual hull code and triangular patch meshes are generated for all possible cases. These meshes are used in conjunction with the TCL script as an input to ANSYS meshing software, which performs re-meshing as described above and outputs the corresponding quadrilateral patch meshes. The quadrilateral meshes are then converted into a suitable format that can be input into the MoM-SIE scattering code, which, in turn, computes and outputs “particle-by-particle” scattering matrices. The final step is a conversion of these matrices into the polarimetric radar observables. The automatic process is outlined in Figure 15.

6. Results and Discussion

First, to test the accuracy of 3D reconstructions based on three cameras (three main, original “internal”, MASC cameras) vs. five cameras (with two additional, “external”, cameras) in Figure 2, simulated images of a sphere with a 3 mm diameter were generated and input into the visual hull code. The sphere was assumed to lie at the exact center of all cameras focal point. At this focal point, the micron resolution of the cameras, which is the size of each pixel in the image in micrometers, is 35.9 μm for the 5 MP cameras and 89.6 μm for the 1.2 MP cameras. This leads to the simulated 3 mm diameter sphere 2D image to have a diameter of approximately 83.5 pixels and 33.5 pixels in the 5 MP, and 1.2 MP cameras, respectively. The computed volume, surface area, aspect ratio, and parameters that relate to the deviation of the 3D points of the reconstructed sphere were compared to the theoretical value. The results are shown in Table 3.

As can be observed from Table 3, the five-camera MASC outperforms the three-camera MASC drastically with lower percent error in every category as well as having an aspect ratio much closer to one. In both cases, the volume and surface area of the reconstructed sphere are overestimates of the actual values. The deviation from surface parameter gives a value relating to how far a node on the reconstructed geometry is from the actual theoretical sphere. A deviation from surface value of 0% indicates the reconstructed node lies exactly on the theoretical sphere’s surface. The camera positions and 3D views of the corresponding sphere reconstructions for the three- and five-camera MASC systems are shown in Figures 16 and 17, respectively. The five-camera reconstruction more closely represents a sphere from the different angles as opposed to the three-camera version, which shows a diamond like shape in some views.

In order to further demonstrate and evaluate the improvement achieved by adding the two upper cameras, Figure 18 shows 3D visual hull reconstructions of several snowflakes of complex shapes, captured at the MASCRAD Field Site (Figure 1), based on photographs from three and five MASC cameras, respectively, along with the computed volume, surface area, and aspect ratio values. As can be observed from the figure, the reconstructions based on five cameras all have smaller volume and surface area than the corresponding three-camera reconstructions. In some cases, as can be seen in Figure 18, the addition of the two cameras drastically changes the reconstructed shape.

Next, to show how well the visual hull method can reconstruct complicated snowflake-like shapes in cases where the actual shapes of the objects are known, fake snowflakes that were 3D printed were dropped through the five-camera MASC. These fake snowflakes were created using 3D CAD modeling, so they have known volumes and surface areas. The images of these objects obtained by the MASC were run through the visual hull code and 3D reconstructions were generated. Sources of error in this method and measurement include the resolution of the 3D printer (50 μm), and the unknown volume and surface errors of the 3D printed snowflakes. Another source is dependent upon at what angle the fake snowflake falls through the MASC and how well it is resolved in each image. Namely, the volume and surface area of the 3D reconstructed snowflake will somewhat vary depending on the orientation angle of the object as it is dropped through the MASC. The reconstructed shapes, their corresponding MASC images, the 2D projections of the 3D reconstructions, as well as comparisons between the volume, surface area, and aspect ratio of the reconstructions and the respective values of the 3D CAD models of 3D printed snowflakes, are shown in Figure 19, where very good results of the visual hull shape reconstruction can be observed in all cases. For reference, Figure 19 also gives the percent error with respect to the CAD models for the volume if the fake snowflakes are reconstructed using a spheroid approximation in place of the visual hull method.

Further, Figure 20 shows 20 examples of 3D reconstructions of different snowflakes or winter precipitation particles collected at the MASC site, near Greeley, Colorado, during a snow event that occurred on February 23rd, 2015. For each particle, the five images (photographs) obtained by the modified MASC system are shown along with the 3D reconstructed shape triangular mesh obtained by the visual hull method and its back projections onto the original images, as well as the information about the volume, surface area, and aspect ratio of the reconstructed snowflake. We observe, from the results, an ability of the presented visual hull method to successfully and accurately perform 3D reconstruction for snowflakes of very realistic, complicated, and diverse shapes and compositions, and very different sizes and complexities, which in addition to demonstrating the power of the visual hull approach, confirms – in experiments involved in a real snow storm observation – availability of sufficient silhouette information from the five cameras of the modified MASC system for 3D reconstruction and excellent mechanical and software self-calibration of the system. We also observe an almost perfect re-projection of the 3D reconstruction of every snowflake and excellent coverage of the projections of the 3D reconstructed geometries as silhouettes onto the original snowflake images (the green areas practically perfectly cover the gray areas for all snowflakes and all five images for each snowflake).

7. Conclusions

This paper has proposed and presented a visual hull method and technique for reconstruction of realistic 3D shapes of snowflakes and other hydrometeors based on high-resolution photographs of particles in freefall from multiple views captured by a multi-angle snowflake camera, or another similar instrument, and the corresponding 2D silhouettes of an object. The results have shown an ability of the method to successfully and accurately perform 3D reconstruction for snowflakes of very realistic, complicated, and diverse shapes and compositions, and very different sizes and complexities – collected at the MASCRAD Field Site, near Greeley, Colorado. The experiments have included demonstrations and evaluations of the improvement achieved by adding the two upper "external" cameras to the three original, "internal", MASC cameras. Tests have been carried out of the accuracy of visual hull 3D reconstructions based on simulated images of a sphere, of a known diameter, as well as on images of 3D printed fake snowflakes of complicated shapes created using 3D CAD modeling, dropped through the improved five-camera MASC, where it is possible to perform comparisons between the volume, surface area, and aspect ratio of the reconstructions and the respective values of the 3D CAD models of 3D printed snowflakes. Very good results of the visual hull shape reconstruction have been observed in all cases, including excellent coverage of the 2D back projections of the 3D reconstructed geometries as silhouettes onto the original snowflake images. All the results, in addition to demonstrating the power of the visual hull approach, have confirmed – in experiments involved in real snow storm observations and those with simulated and fake 3D printed snowflakes – availability of sufficient silhouette information from the five cameras of the modified MASC system for 3D reconstruction and excellent mechanical and software self-calibration of the system.

This is the first time reconstructions of 3D hydrometeor shapes of winter precipitation based on multiple high-resolution photographs of real (measured) snowflakes are performed. When compared to other existing methods and techniques for generating geometrical and physical models of the winter precipitation particles based on observations by advanced optical imaging disdrometers, the results presented in this paper are clearly much better than any snowflake 3D realistic-shape reconstruction data in the literature. In particular, when compared to the work in Teschl et al. (2006), the horizontal resolution of the 2DVD for the current production model is 150 μm, which is insufficient to capture details of the complexity of ice particles, and there is, of course, a distinct advantage provided by photographs with respect to the 2DVD contours. The MASC camera resolution is three or more times higher than the 2DVD resolution and the MASC also has more angles of view, and both these facts allow for the visual hull method to provide more detailed reconstructions than the method used by Teschl et al. (2006). For the similar reasons, the MASC/visual hull approach is substantially advantageous over the ellipsoid models of snow particles obtained from 2DVD contour images in Huang et al. (2014). When compared to the work in Garret et al. (2012), by use of the visual hull method we are able to relate all the images in a set together and create a reconstruction that conforms to all the different angular views of the snowflake. This provides a much more accurate 3D reconstruction of the snowflake than the model obtained by extruding the 2D silhouette of a single MASC image in Garret et al. (2012).

Although this paper has presented the methodology and technique for reconstruction of realistic 3D shapes of snowflakes and other hydrometeors based on MASC images, it can be adapted for use in conjunction with any other instrument providing high-resolution photographs of particles in freefall from multiple views. In addition, while the results in the paper are mostly for the snowflake shape reconstructions using five photographs of a hydrometeor collected by five cameras of the improved five-camera MASC system, the proposed technique can be applied to any number of photographs obtained by any number of cameras that provide sufficient spatial information about the object for the desired or sufficient accuracy of the reconstruction.

In addition to enabling realistic computation of "particle-by-particle" scattering matrices and polarimetric radar measurables for winter precipitation, the 3D shape reconstructions of hydrometeors by the proposed visual hull technique, in conjunction with the MASC or another similar instrument, can as well be used for studies of snow habits, for advanced analyses of microphysical characteristics of particles, and for hydrometeor classification. Finally, more accurate and realistic estimates of the particle volume, mass, and density, in conjunction with measurements of the particle size distribution (PSD), can significantly improve the radar-based estimation of liquid equivalent snow rates near the surface.

Future work will include MASC/visual-hull/meshing/scattering analyses of data collected at multiple snow events observed at the MASCRAD Field Site, as well as studies of microphysical characteristics of particles mentioned above.

Acknowledgment

This work was supported by the National Science Foundation under Grant AGS-1344862.

References

Andrić, J., M. R. Kumjian, D. S. Zrnić, J. M. Straka, and V. M. Melnikov, 2012: Polarimetric signatures above the melting layer in winter storms: An observational and modeling study. Early on-line release, *Journal of Applied Meteorology and Climatology*, doi: http://dx.doi.org/10.1175/JAMC-D-12-028.1

ANSYS ICEM CFD, 2014: http://resource.ansys.com/Products/Other+Products/ANSYS+ICEM+CFD

Bader, M. MB – Ruler the Triangula Screen Ruler, http://www.markus-bader.de/MB-Ruler/index.php.

Barthazy, E., S. Göke, R. Schefold, and D. Högl, 2004: An optical array instrument for shape and fall velocity measurements of hydrometeors. *J. Atmos. Oceanic Technol*., vol. **21**, 1400–1416.

Baumgart, B. G., 1974: Geometric modeling for computer vision. Ph.D. Thesis, Computer Science Department, Stanford University.

Bloomenthal, J., 1994: An Implicit Surface Polygonizer, The University of Calgary, Calgary, Alberta T2N 1N4 Canada.

Böhm, H. P., 1989: A general equation for the terminal fall speed of solid hydrometeors. *J. Atmos. Sci*., vol. **46**, 2419–2427.

Bringi, V. N., B. Notaroš, C. Kleinkort, G.-J. Huang, M. Thurai, and P. Kennedy, 2015: Comprehensive Analysis of an Unusual Winter Graupel Shower Event Recorded by an S-Band

Polarimetric Radar and Two Optical Imaging Surface Instruments. *American Meteorological Society's 37th Conference on Radar Meteorology*, 14-18 September, 2015, Norman, OK.

Chobanyan E., N. J. Sekeljiic, A. B. Manic, M. M. Ilic, V. N. Bringi, and B. M. Notaroš, 2015: Efficient and Accurate Computational Electromagnetics Approach to Precipitation Particle Scattering Analysis Based on Higher Order Method of Moments Integral-Equation Modeling. *J. Atmos. Oceanic Technol.*, vol. **32**, 1745–1758.

Djordjević, M. and B. M. Notaroš, 2004: Double higher order method of moments for surface integral equation modeling of metallic and dielectric antennas and scatterers. *IEEE Transactions on Antennas and Propagation*, vol. **52**, no. 8, 2118−2129.

Du, J., J. Shi, and H. Rott, 2010: Comparison between a multi-scattering and multi-layer snow scattering model and its parameterized snow backscattering model. *Remote Sensing of Environment*, vol. **114**, 1089–1098.

Evans, K. F., and G. Stephens, 1995: Microwave radiative transfer through clouds composed of realistically shaped ice crystals. Part I: Single scattering properties. J. *Atmos. Sci.*, vol. **52**, 2041–2057.

Fischler, M. A. and R. C. Bolles, 1981: Random sample consensus: A paradigm for model fitting with applications to image analysis and automated cartography., *Commun. ACM*, vol. **24**, 381-395.

Forbes, K., 2007: Calibration, recognition, and shape from silhouettes of stones. *PhD thesis, Department of Electrical Engineering, University of Cape Town*, Cape Town, South Africa.

Garrett, T. J., C. Fallgatter, K. Shkurko, and D. Howlett, 2012: Fallspeed measurement and high-resolution multi-angle photography of hydrometeors in freefall. *Atmos. Meas. Tech. Discuss*., vol. **5**, 4827−4850, doi:10.5194/amtd-5-4827-2012.

Grecu, M., and W. Olson, 2008: Precipitating snow retrievals from combined airborne cloud radar and millimeter-wave radiometer observations. *J. Appl. Meteor. Climatol.*, vol. **47**, 1634–1650.

Hartley, R. and A. Zisserman, 2000: *Multiple view geometry in computer vision*. Cambridge University Press, Cambridge, UK.

Hong, G., 2007a: Parameterization of scattering and absorption properties of nonspherical ice crystals at microwave frequencies, *Journal of Geophysical Research*, vol. **112**, D11208, doi:10.1029/2006JD008364.

Hong, G., 2007b: Radar backscattering properties of nonspherical ice crystals at 94 GHz. *J. Geophys*. Res., vol. **112**, D22203. doi:10.1029/2007JD008839.

Huang, G., V. N. Bringi, D. Moisseev, W. A. Petersen, L. Bliven, and D. Hudak, 2015: Use of 2D-Video Disdrometer to Derive Mean Density-Size and Ze-SR Relations: Four Snow Cases from the Light Precipitation Validation Experiment. *Atmospheric Research,* vol. **153**, 34-48.

Ishimoto, H., 2008: Radar Backscattering Computations for Fractal-Shaped Snowflakes. *Journal of the Meteorological Society of Japan*, vol. **86**, 459-469.

Kennedy, P. C. and S. A. Rutledge, 2011: S-Band Dual-Polarization Radar Observations of Winter Storms. *J. Appl. Meteor. Climatol*., vol. **50**, 844–858.

Kennedy, P. C., C. Kleinkort, G.-J. Huang, M. Thurai, A. Newman, J. Hubbert, S. Rutledge, V. N. Bringi, and B. M. Notaroš, 2015: Preliminary Results from the Multi-Angle Snowflake Camera and Radar (MASCRAD) Project. *American Meteorological Society's 37th Conference on Radar Meteorology*, 14-18 September, 2015, Norman, OK.

Kim, M. J., 2006: Single scattering parameters of randomly oriented snow particles at microwave frequencies, *Journal of Geophysical Research*, col. 111, D14201, doi:10.1029/2005JD006892.

Kim, M., M. Kulie, C. O'Dell, and R. Bennartz, 2007: Scattering of ice particles in microwave frequencies: A physically based parameterization. *J. Appl. Meteor. Climatol.*, vol. **46**, 615–633.

Kleinkort, C., G.-J. Huang, E. Chobanyan, A. Manic, M. Ilic, A. Pezeshki, V. N. Bringi, and B. Notaros, 2015a: Visual Hull Method Based Shape Reconstruction of Snowflakes from MASC Photographs. *Proceedings of the 2015 IEEE International Symposium on Antennas and Propagation and North American Radio Science Meeting*, July 19-25, 2015, Vancouver, BC, Canada, 1122–1123.

Kleinkort, C., G.-J. Huang, S. Manic, A. Manic, P. Kennedy, J. Hubbert, A. Newman, V. N. Bringi, and B. Notaroš, 2015b: 3D Shape Reconstruction of Snowflakes from Multiple Images, Meshing, Dielectric Constant Estimation, Scattering Analysis, and Validation by Radar Measurements. *American Meteorological Society's 37th Conference on Radar Meteorology*, 14-18 September, 2015, Norman, OK (*Winner of The Spiros G. Geotis Student Prize*).

Kneifel, S., U. Löhnert, A. Battaglia, S. Crewell, and D. Siebler, 2010: Snow scattering signals in round based passive microwave radiometer measurements. *Journal of Geophysical Research*, vol. **115**, D16214, doi:10.1029/2010JD013856.

Kuo, K., W. Olson, B. Johnson, M. Grecu, L. Tian, T. Clune, B. van Aartsen, A. Heymsfield, L. Liao, and R. Meneghini, 2016: The Microwave Radiative Properties of Falling Snow Derived from Nonspherical Ice Particle Models. Part I: An Extensive Database of Simulated Pristine Crystals and Aggregate Particles, and Their Scattering Properties. *Journal of Applied Meteorology and Climatology*, vol. **55**, 691-708.

Laurentini, A., 1994: The visual hull concept for silhouette-based image understanding. *IEEE Transaction on Pattern Analysis and Machine Intelligence,* vol. **16**, no. 2, 150−162.

Laurentini, A., 1995: How far 3D shapes can be understood from 2D Silhouettes. *IEEE Transaction on Pattern Analysis and Machine Intelligence,* vol. **17**, no. 2, 188−195.

Leinonen, J., D. Moisseev, and T. Nousiainen, 2013: Linking snowflake microstructure to multi-frequency radar observations. *Journal of Geophysical Research*, vol. **118**, 3259–3270.

Leinonen J. and W. Szyrmer, 2015: Radar signatures of snowflake riming: a modeling study. *Earth and Space Science*, vol. **2**, 346–358.

Liu, G., 2008: A Database of Microwave Single-Scattering Properties for Nonspherical Ice Particles. BAMS, October 2008, 1564–1570.

Liu, G., 2010: Approximation of Single Scattering Properties of Ice and Snow Particles for High Microwave Frequencies. *Journal of the Atmospheric Sciences*, vol. **61**, 2441–2456.

Mason, B. J., 2010: The Physics of Clouds. *Oxford University Press*.

Matrosov, S. Y., C. Campbell, D. Kingsmill, and E. Sukovich, 2009: Assessing Snowfall Rates from X-Band Radar Reflectivity Measurements. *J. Atmos. Oceanic Technol*., vol. **26**, 2324–2339.

Matrosov, S. Y., R. F. Reinking, R. A. Kropfli, B. E. Martner, and B. W. Bartram, 2001: On the Use of Radar Depolarization Ratios for Estimating Shapes of Ice Hydrometeors in Winter Clouds. *J. Appl. Meteor*., vol. **40**, 479–490.

Matusik, W., C. Buehler, R. Raskar, L. McMillan, and S. Gortler, 2000: Image-Based Visual Hulls. *Proceedings of SIGGRAPH 2000*.

Maxwell-Garnet, J. C., 1904: Colors in metal glasses and in metallic films., Phil. Trans. Roy. Soc., A203, 385-420.

Newman, A. J., P. A. Kucera, and L. F. Bliven, 2009: Presenting the Snowflake Video Imager (SVI), *Journal of Atmospheric and Oceanic Technology*, vol. **26**:2, 167-179.

Notaros B., V. N. Bringi, C. Kleinkort, G.-J. Huang, E. Chobanyan, M. Thurai, O. Notaros, A. Manic, A. Newman, P. Kennedy, J. Hubbert, T. Lim, W. Brown, and M. Ilic, 2015a: Measurement and Characterization of Winter Precipitation at MASCRAD Snow Field Site. *Proceedings of the 2015 IEEE International Symposium on Antennas and Propagation and North American Radio Science Meeting*, July 19-25, 2015, Vancouver, BC, Canada, 979–980.

Notaros, B. M., V. N. Bringi, A. J. Newman, C. Kleinkort, G.-J. Huang, P. Kennedy, and M. Thurai, 2015b: Accurate Characterization of Winter Precipitation Using In-Situ Instrumentation, CSU-CHILL Radar, and Advanced Scattering Methods. *2015 AGU Fall Meeting*, 14-18 December 2015, San Francisco, CA.

Notaroš, B. M., V. N. Bringi, E. Chobanyan, C. Kleinkort, S. B. Manic, N. J. Sekeljic, A. B. Manic, and M. M. Ilic, 2015c: Computation of Particle Scattering Matrices and Polarimetric Radar Variables for Winter Precipitation Using T-Matrix Method, DDA Method, and Higher Order MoM-SIE Method. *American Meteorological Society's 37th Conference on Radar Meteorology*, 14-18 September, 2015, Norman, OK.

Notaroš, B. M., V. N. Bringi, C. Kleinkort, P. Kennedy, G.-J. Huang, M. Thurai, A. J. Newman, W. Bang, and G. Lee, 2016: Accurate Characterization of Winter Precipitation Using Multi-Angle Snowflake Camera, Visual Hull, Advanced Scattering Methods and Polarimetric Radar. *Invited paper*, Special Issue Advances in Clouds and Precipitation, *Atmosphere*, vol. **7**, no. 6, 81–111.

Petty, G. and W. Huang, 2010: Microwave Backscatter and Extinction by Soft Ice Spheres and Complex Snow Aggregates. *J. Atmos. Sci.*, vol. **67**, 769–787.

Pruppacher, H. R. and Klett, J. D., 2010: Microphysics of Clouds and Precipitation. (Second revised and expanded edition) *Series: Atmospheric and Oceanographic Sciences Library*, Vol. 18, *Springer*.

Reinking, R. F., S. Y. Matrosov, R. A. Kropfli, and B. W. Bartram, 2002: Evaluation of a 45° Slant Quasi-Linear Radar Polarization State for Distinguishing Drizzle Droplets, Pristine Ice Crystals, and Less Regular Ice Particles. *J. Atmos. Oceanic Technol.*, vol. **19**, 296–321.

Ryzhkov, A. V., D. S. Zrnic, and B. A. Gordon, 1998: Polarimetric Method for Ice Water Content Determination. *J. Appl. Meteor.*, vol. **37**, 125–134.

Sobel, I., 1970: Camera models and machine perception., Ph. D Dissertation, Artificial Intelligence Lab. Stanford University, **AIM-21**.

Straka, J., D. S. Zrnić, and A. V. Ryzhkov, 2000: Bulk hydrometeor classification and quantification using polarimetric radar data: Synthesis of Relations. *J. Appl. Meteor.*, vol. **39**, 1341–1372.

Sturm, P., B. Triggs, 1996: A Factorization Based Algorithm for Multi-Image Projective Structure and Motion. *4th European Conference on Computer Vision*, Cambridge, England, 709-720.

Svoboda, T., Martinec, D. and Pajdla, T., A convenient multi-camera self-calibration for virtual environments., PRESENCE: *Teleoperators and Virtual Environments*, Vol. **14**, (4), pp 407-422, August 2005. MIT Press.

Teschl, F., W. L. Randeu, and M. Schönhuber, 2006: Modelling microwave scattering by solid precipitation particles. *Proceedings of The European Conference on Antennas and Propagation: EuCAP 2006*, Nice, France, 310.1−310.5.

Tyynelä, J., J. Leinonen, D. Moisseev, and T. Nousiainen, 2011: Radar Backscattering from Snowflakes: Comparison of Fractal, Aggregate, and Soft Spheroid Models. *J. Atmos. Oceanic Technol.*, vol. **28**, 1365–1372.

VHMC Software: Visual Hull Mesh Code, 2012: http://www.dip.ee.uct.ac.za/~kforbes/DoubleMirror/DoubleMirror.html

Vivekanandan, J., V. N. Bringi, M. Hagen, and P. Meischner, 1994: Polarimetric radar studies of atmospheric ice particles. *Trans. IEEE Geosci Remote Sens*, vol. **32**, No. 1, 1−10.

Westbrook, C., R. C. Ball, and P. R. Field, 2006: Radar scattering by aggregate snowflakes, *Quart. J. Roy. Meteor. Soc.*, **132**, 897–914.

Westbrook, C. D., 2008: The fall speeds of sub-100 μm ice crystals, *Quart. J. Roy. Meteor. Soc.*, **134**, 1243–1251.

Yang, P., H. Wei, H.-L. Huang, B. A. Baum, Y. X. Hu, G. W. Kattawar, M. I. Mishchenko, and Q. Fu, 2005: Scattering and absorption property database for nonspherical ice particles in the near- through far-infrared spectral region. *Appl. Opt.*, vol. **44**, 5512–5523.

Yang, P., L. Bi, B. A. Baum, K. Liou, G. W. Kattawar, M. I. Mishchenko and B. Cole, 2013: Spectrally Consistent Scattering, Absorption, and Polarization Properties of Atmospheric Ice Crystals at Wavelengths from 0.2 to 100 μm., *J. Atmos. Sci.*, vol. **70**, 330-347.

Zhang, G., S. Luchs, A. Ryzhkov, M. Xue, L. Ryzhkova, and Q. Cao, 2011: Winter Precipitation Microphysics Characterized by Polarimetric Radar and Video Disdrometer Observations in Central Oklahoma. *J. Appl. Meteor. Climatol*., vol. **50**, 1558–1570.

Tables

Table 1. Azimuthal and elevation angles of all five cameras in the new MASC system, in Figure 2.

	Azimuth [degrees]	Elevation [degrees]
Camera 1 (original)	0	0
Camera 2 (original)	36	0
Camera 3 (original)	72	0
Camera 4 (addition)	144	55
Camera 5 (addition)	288	55

Table 2. Description of variables used in intrinsic camera parameter equations, resulting in estimates for a starting point in the self-calibration software.

M_{res}	$Micron\ Resolution$
R	$Resolution\ (number\ of\ pixels\ 1D)$
FOV	$Field\ of\ View$
AOV	$Angle\ of\ View$
P_s	$Pixel\ Size\ (parameter\ of\ CCD)$
d_s	$Distance\ to\ Subject\ (working\ distance)$
d_f	$Sensor\ Size(1D)$
f	$Effective\ Focal\ Length$
P_p	$Pixel\ Pitch$
DOF	$Depth\ of\ Field$

Table 3. Comparison of sphere reconstruction based on the original three-camera MASC and the new five-camera MASC (Figure 2).

	3 Camera	5 Camera
Volume [% Error]	27.03	5.31
Surface Area [% Error]	27.35	6.43
Aspect Ratio	0.5974	0.8569
Average Deviation of Nodes from Surface [% Error]	12.45	2.54
Maximum Deviation of Nodes from Surface [% Error]	66.79	26.98
Standard Deviation of Nodes [mm]	0.25	0.064
Percent Nodes < 10% Error from Surface	65.19	92.91
Percent Nodes < 5% Error from Surface	56.10	85.37
Percent Nodes < 1% Error from Surface	26.10	51.72

Figure Caption List

Figure 1. MASCRAD Snow Field Site at Easton Valley View Airport, near Greeley, Colorado: 2/3-scaled double fence intercomparison reference (DFIR) wind shield housing various surface instrumentation; shown are a multi-angle snowflake camera (MASC), a two-dimensional video disdrometer (2DVD), a Pluvio snow measuring gauge, and a meteorological particle spectrometer (MPS). These instruments operate under the umbrella of CSU-CHILL Radar.

Figure 2. Multi-angle snowflake camera (MASC), with three cameras in horizontal plane for capturing high-resolution photographs of snowflakes in freefall and measuring their fall speed; CSU MASC system has two added "external" cameras (in temperature controlled enclosures) on an elevated plane, at about a 55° angle above horizon, to improve 3D reconstruction of snowflakes.

Figure 3. Three example sets, in three horizontal panels, of five photographs of three different snowflakes collected by five cameras of the new five-camera MASC system, in Figure 2, at the MASCRAD Field Site, in Figure 1. Each hydrometeor, in each horizontal panel, is imaged from five different views.

Figure 4. Illustration of visual hull method with three cameras and their corresponding silhouettes projected and intersected with each other to obtain a 3D shape reconstruction of a hydrometeor.

Figure 5. Mean (top) and standard deviation (bottom) of MASC background images for five cameras over one hour period on December 26th, 2014, hour 18 UTC. A total of 237 images were used in calculating the mean and standard deviation in this case.

Figure 6. Examples of multiple-snowflake images recorded by the MASC from varying snow events, on December 26th, 2014 (left panel), February 16th, 2015 (central panel), and March 3rd, 2015 (right panel), respectively.

Figure 7. Set of MASC images with snowflakes boxed and corresponding number observed in each image. Camera that contains the least number of snowflakes is used as starting image for visual hull, Cam 5 in this example. The snowflakes were observed on March 3rd, 2015.

Figure 8. Starting image, Camera 5 from Figure 7, split into 3 individual images with only one snowflake per image.

Figure 9. Example of the visual hull 3D reconstruction of a snowflake (right) based on five MASC images (top left); the corresponding 2D re-projections of the 3D reconstructed shape onto images are also shown (bottom left). The unit of the grid is mm.

Figure 10. Visual hull 3D reconstructions of the same snowflake shown in Figure 9 using several decreasing voxel sizes. Number of triangular elements, volume (V), surface area (SA), and aspect ratio (AR) are given for each reconstruction. The unit of the grid is mm.

Figure 11. Convergence of volume (left panel), surface area (central panel), and aspect ratio (right panel) of a random set of 150 snowflake reconstructions with a decreasing voxel size (increasing level of refinement).

Figure 12. Calibration grid used in the mechanical calibration for the five cameras (three main, original "internal", MASC cameras and two additional, "external", cameras,,Figure 2): matching of the physical calibration grid in camera's working volume with the grid on computer screen.

Figure 13. 2D re-projections (green areas) of the 3D reconstruction of a snowflake over the images (gray areas) from the three original MASC cameras. Coverage of projections is poor due to an imperfect calibration of the camera system.

Figure 14. Visual hull 3D reconstructions of hydrometeors, shown in green, represented using triangular patches and the corresponding conversion of the reconstructions to quadrilateral meshes, shown in purple, using ANSYS meshing software.

Figure 15. Outline of steps of the automatic MASC/visual-hull/meshing/scattering observation/analysis process for each collected and analyzed snowflake starting from collection of data to computation of radar observables.

Figure 16. (three left panels) Three-camera sphere reconstruction viewed from three different spatial directions defined by (azimuth angle, elevation angle). (right-most panel) Spatial

positions of the three cameras and their FOV intersection, i.e., measurement volume. The unit of the grid is mm.

Figure 17. The same as in Fig. 16 but for five-camera sphere reconstruction.

Figure 18. 3D reconstructions of five different recorded snowflakes based on three-camera (top panels) and five-camera (bottom panels) MASC instruments. For each reconstruction, the corresponding computed volume (V), surface area (SA), and aspect ratio (AR) are given as well. The unit of the grid is mm.

Figure 19. Visual hull reconstructions of 3D printed fake snowflakes and the corresponding MASC images, along with the projections of 3D reconstructed shapes onto 2D images. Percent errors of the volume (V), surface area (SA), and aspect ratio (AR) of the 3D reconstructions relative to the V, SA, and AR values of the 3D CAD models of 3D printed snowflakes are given as well. The volume percent error with respect to the V of the CAD models is shown also for the reconstructions of fake snowflakes using spheroids instead of the visual hull method.

Figure 20. 20 examples of 3D visual hull reconstructions of different snowflakes collected at the MASCRAD Field Site (Fig. 1) during a February 23rd, 2015 snow event. For each snowflake, the five photographs from the modified MASC system (Fig. 2) are shown along with the 3D reconstructed shape triangular mesh and its back projections onto the original images. To the right of each 3D reconstruction, the calculated volume (V), surface area (SA), and aspect ratio (AR) of the mesh are given as well. The unit of the grid is mm.

Figures

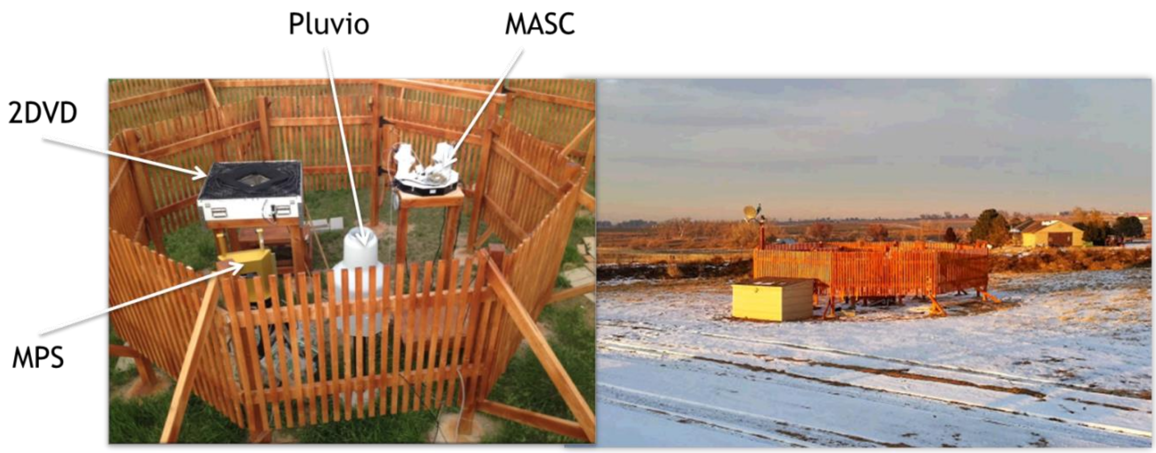

Figure 1. MASCRAD Snow Field Site at Easton Valley View Airport, near Greeley, Colorado: 2/3-scaled double fence intercomparison reference (DFIR) wind shield housing various surface instrumentation; shown are a multi-angle snowflake camera (MASC), a two-dimensional video disdrometer (2DVD), a Pluvio snow measuring gauge, and a meteorological particle spectrometer (MPS). These instruments operate under the umbrella of CSU-CHILL Radar.

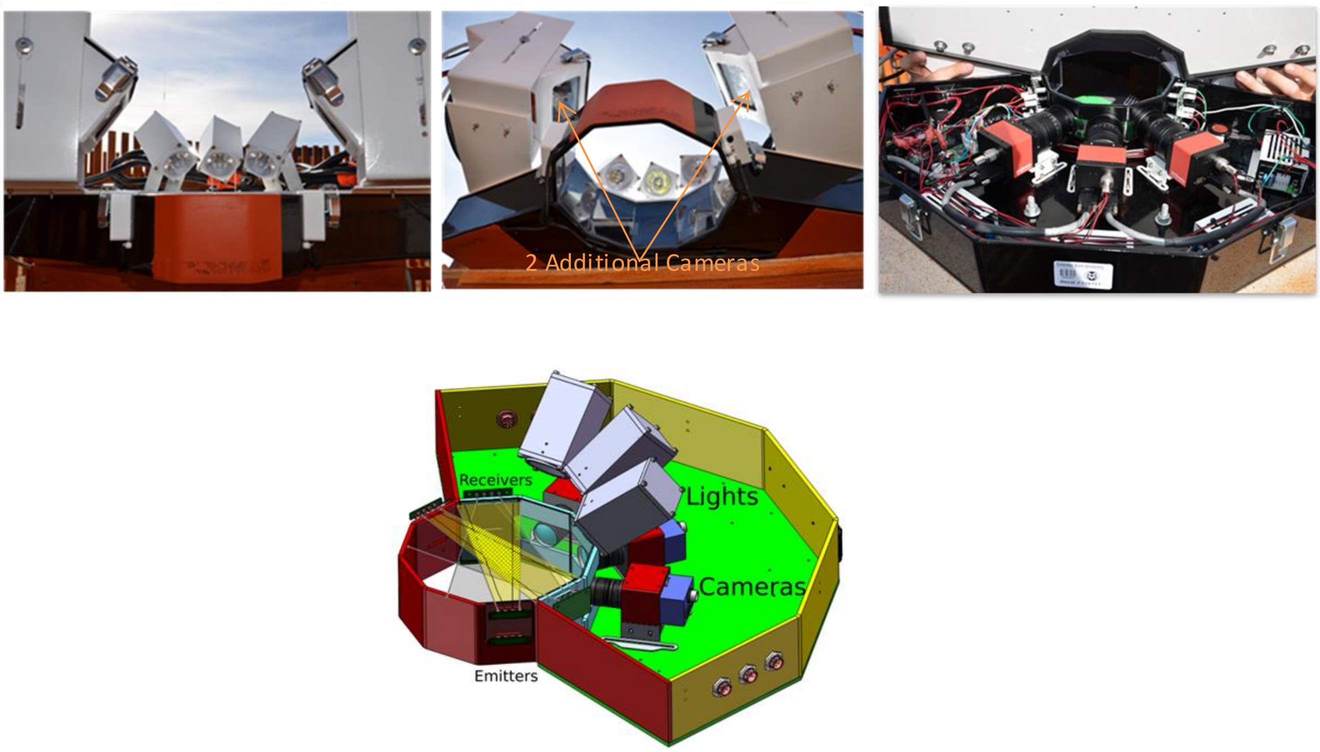

Figure 2. Multi-angle snowflake camera (MASC), with three cameras in horizontal plane for capturing high-resolution photographs of snowflakes in freefall and measuring their fall speed; CSU MASC system has two added "external" cameras (in temperature controlled enclosures) on an elevated plane, at about a 55° angle above horizon, to improve 3D reconstruction of snowflakes.

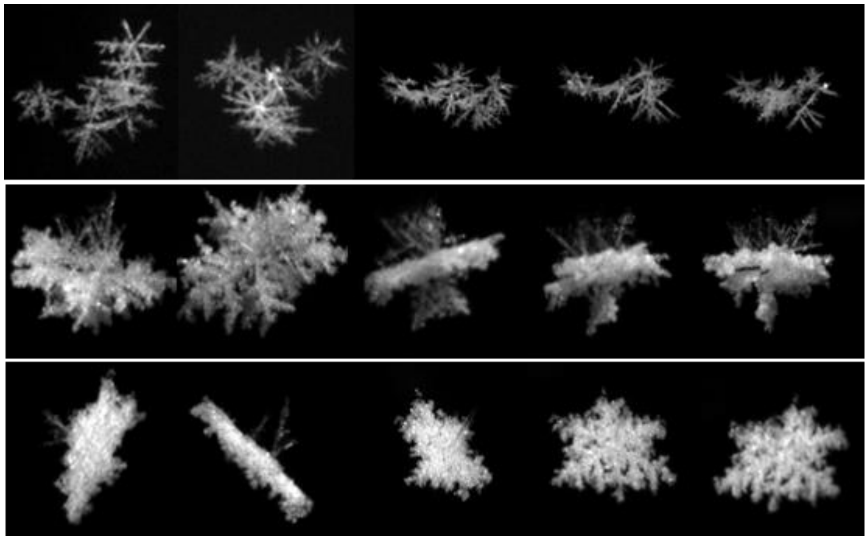

Figure 3. Three example sets, in three horizontal panels, of five photographs of three different snowflakes collected by five cameras of the new five-camera MASC system, in Figure 2, at the MASCRAD Field Site, in Figure 1. Each hydrometeor, in each horizontal panel, is imaged from five different views.

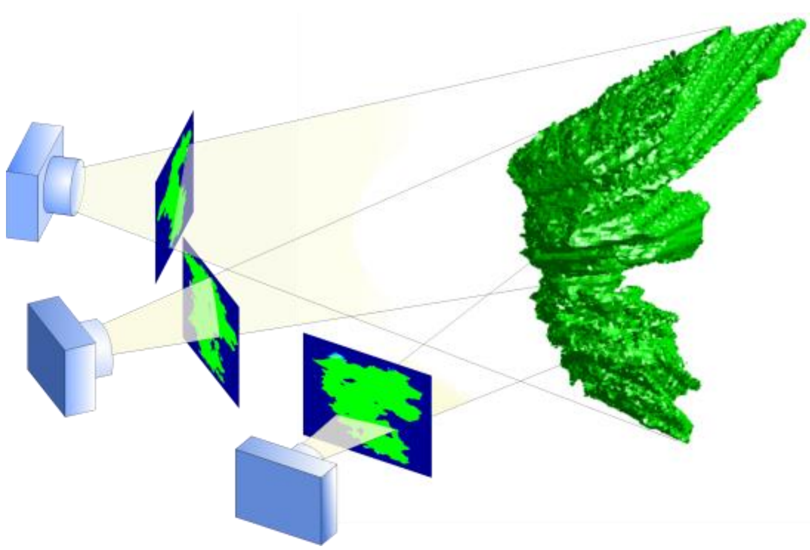

Figure 4. Illustration of visual hull method with three cameras and their corresponding silhouettes projected and intersected with each other to obtain a 3D shape reconstruction of a hydrometeor.

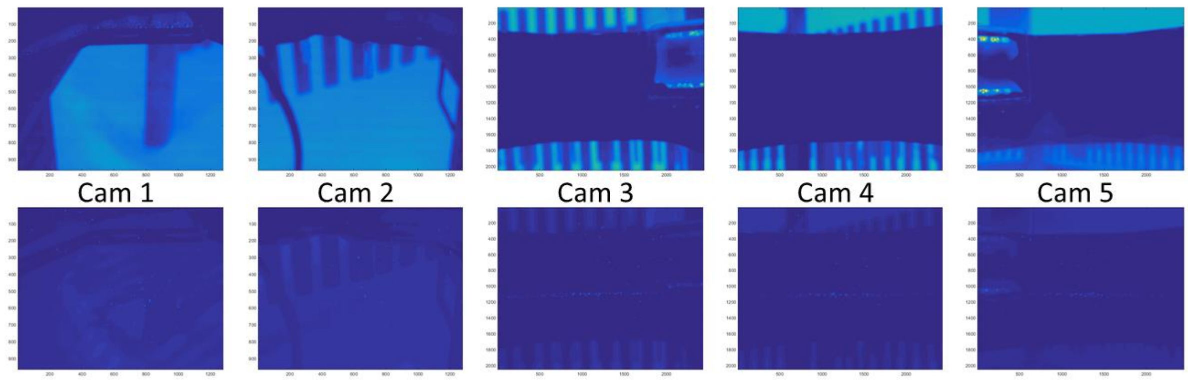

Figure 5. Mean (top) and standard deviation (bottom) of MASC background images for five cameras over one hour period on December 26th, 2014, hour 18 UTC. A total of 237 images were used in calculating the mean and standard deviation in this case.

Figure 6. Examples of multiple-snowflake images recorded by the MASC from varying snow events, on December 26th, 2014 (left panel), February 16th, 2015 (central panel), and March 3rd, 2015 (right panel), respectively.

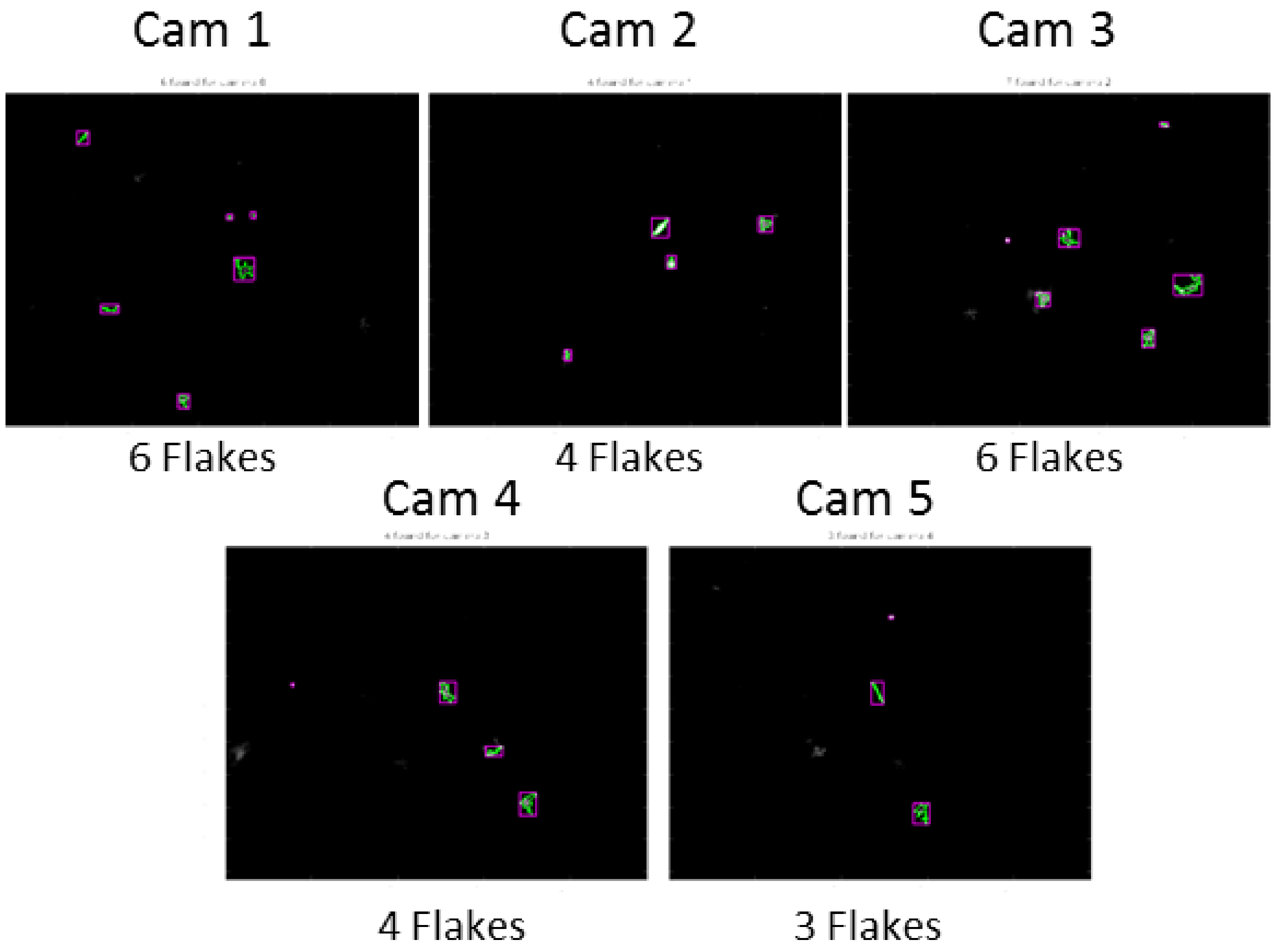

Figure 7. Set of MASC images with snowflakes boxed and corresponding number observed in each image. Camera that contains the least number of snowflakes is used as starting image for visual hull, Cam 5 in this example. The snowflakes were observed on March 3rd, 2015.

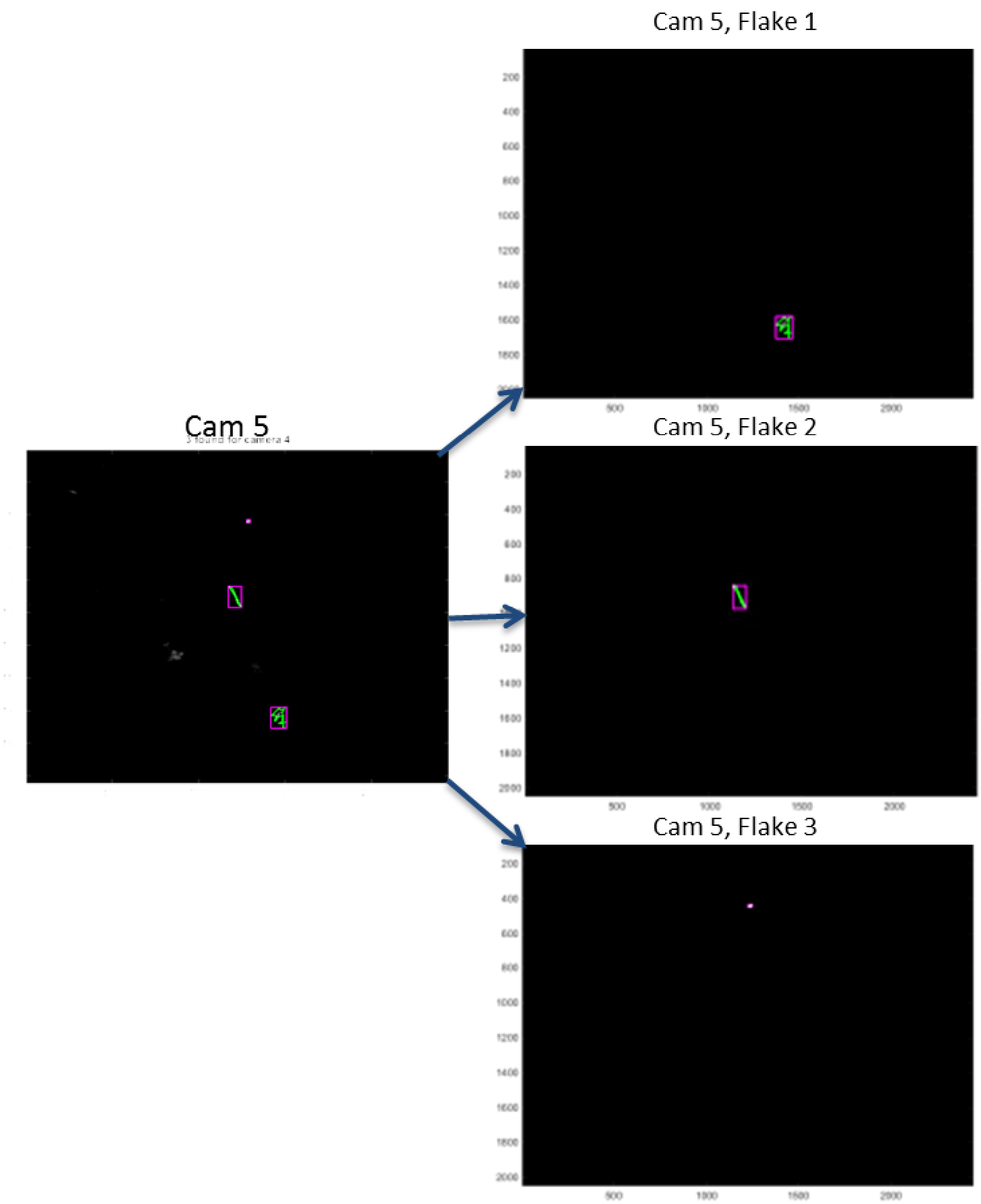

Figure 8. Starting image, Camera 5 from Figure 7, split into 3 individual images with only one snowflake per image.

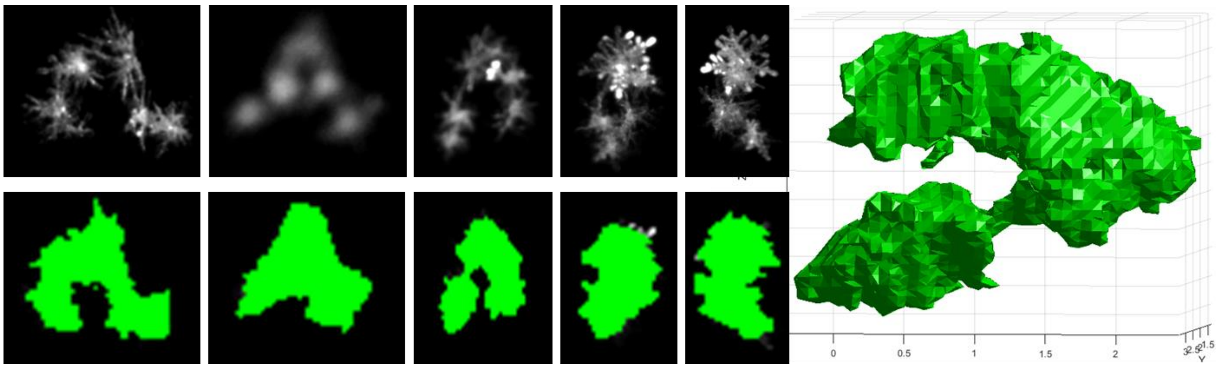

Figure 9. Example of the visual hull 3D reconstruction of a snowflake (right) based on five MASC images (top left); the corresponding 2D re-projections of the 3D reconstructed shape onto images are also shown (bottom left). The unit of the grid is mm.

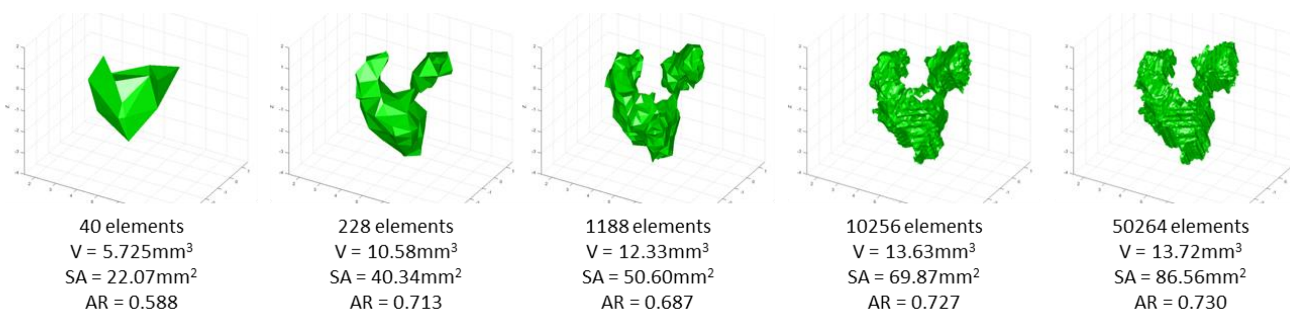

Figure 10. Visual hull 3D reconstructions of the same snowflake shown in Figure 9 using several decreasing voxel sizes. Number of triangular elements, volume (V), surface area (SA), and aspect ratio (AR) are given for each reconstruction. The unit of the grid is mm.

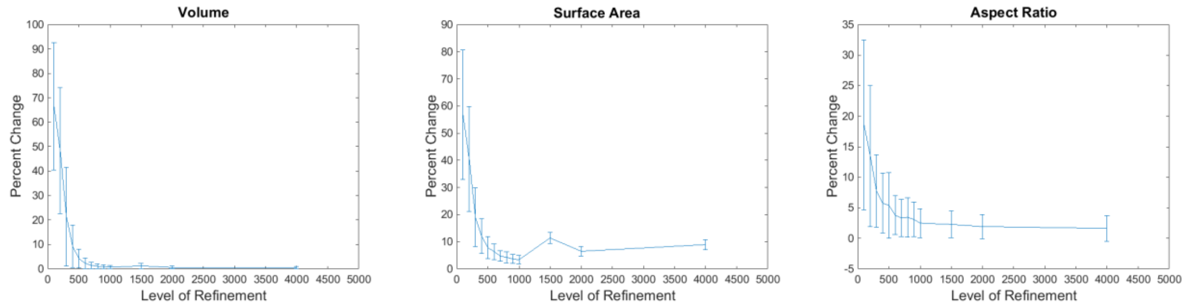

Figure 11. Convergence of volume (left panel), surface area (central panel), and aspect ratio (right panel) of a random set of 150 snowflake reconstructions with a decreasing voxel size (increasing level of refinement).

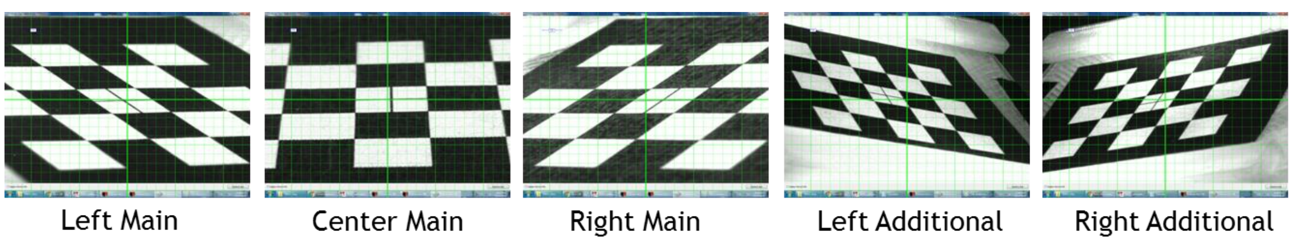

Figure 12. Calibration grid used in the mechanical calibration for the five cameras (three main, original “internal”, MASC cameras and two additional, “external”, cameras, Figure 2): matching of the physical calibration grid in camera’s working volume with the grid on computer screen.

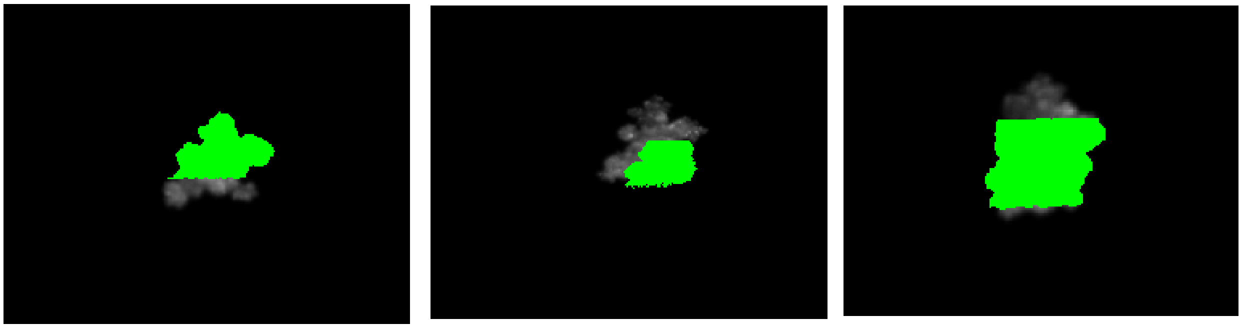

Figure 13. 2D re-projections (green areas) of the 3D reconstruction of a snowflake over the images (gray areas) from the three original MASC cameras. Coverage of projections is poor due to an imperfect calibration of the camera system.

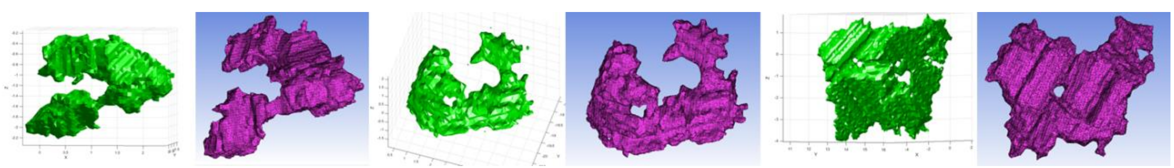

Figure 14. Visual hull 3D reconstructions of hydrometeors, shown in green, represented using triangular patches and the corresponding conversion of the reconstructions to quadrilateral meshes, shown in purple, using ANSYS meshing software.

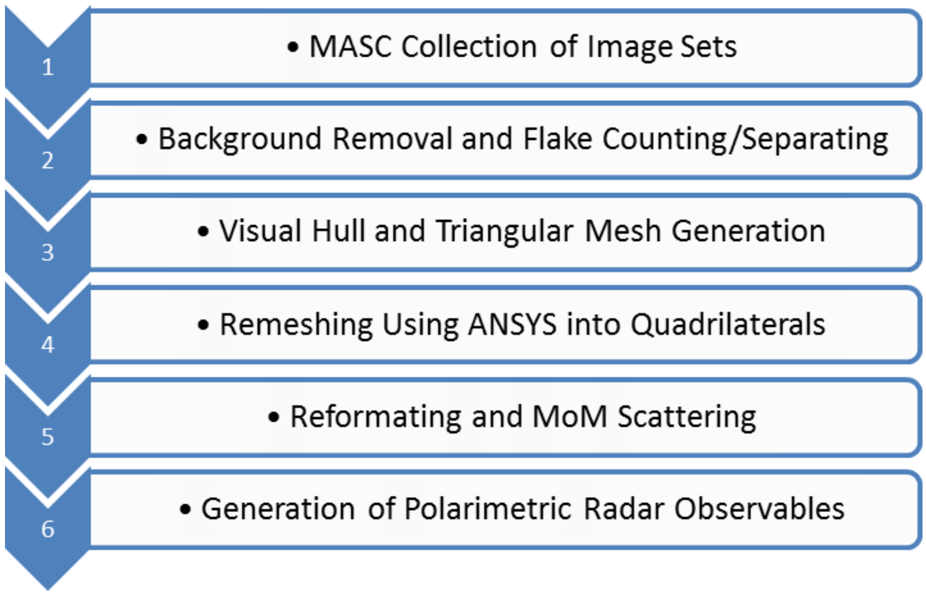

Figure 15. Outline of steps of the automatic MASC/visual-hull/meshing/scattering observation/analysis process for each collected and analyzed snowflake starting from collection of data to computation of radar observables.

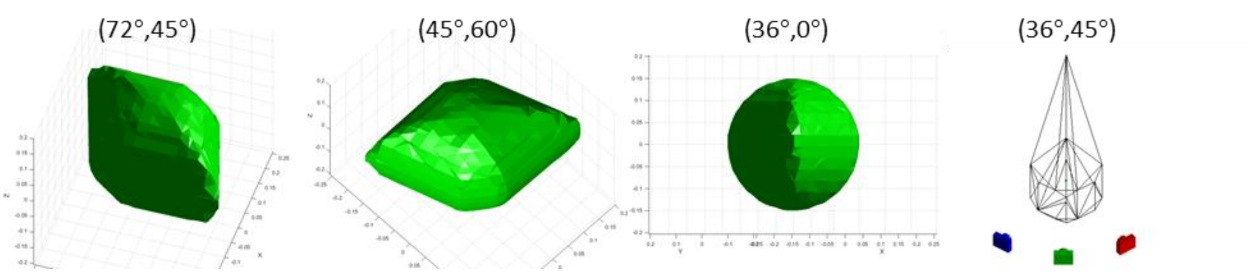

Figure 16. (three left panels) Three-camera sphere reconstruction viewed from three different spatial directions defined by (azimuth angle, elevation angle). (right-most panel) Spatial positions of the three cameras and their FOV intersection, i.e., measurement volume. The unit of the grid is mm.

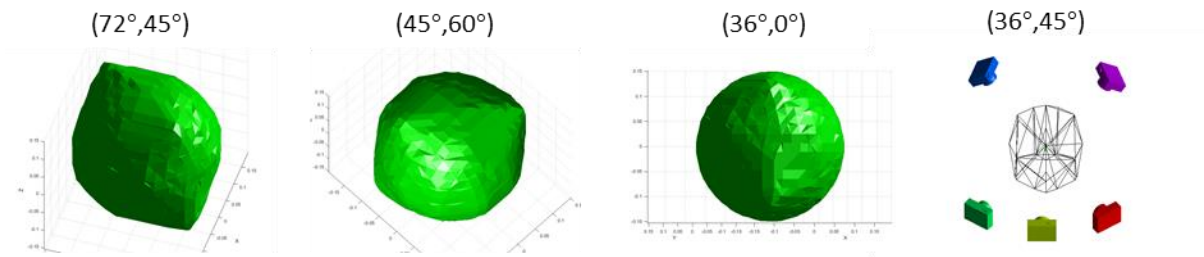

Figure 17. The same as in Fig. 16 but for five-camera sphere reconstruction.

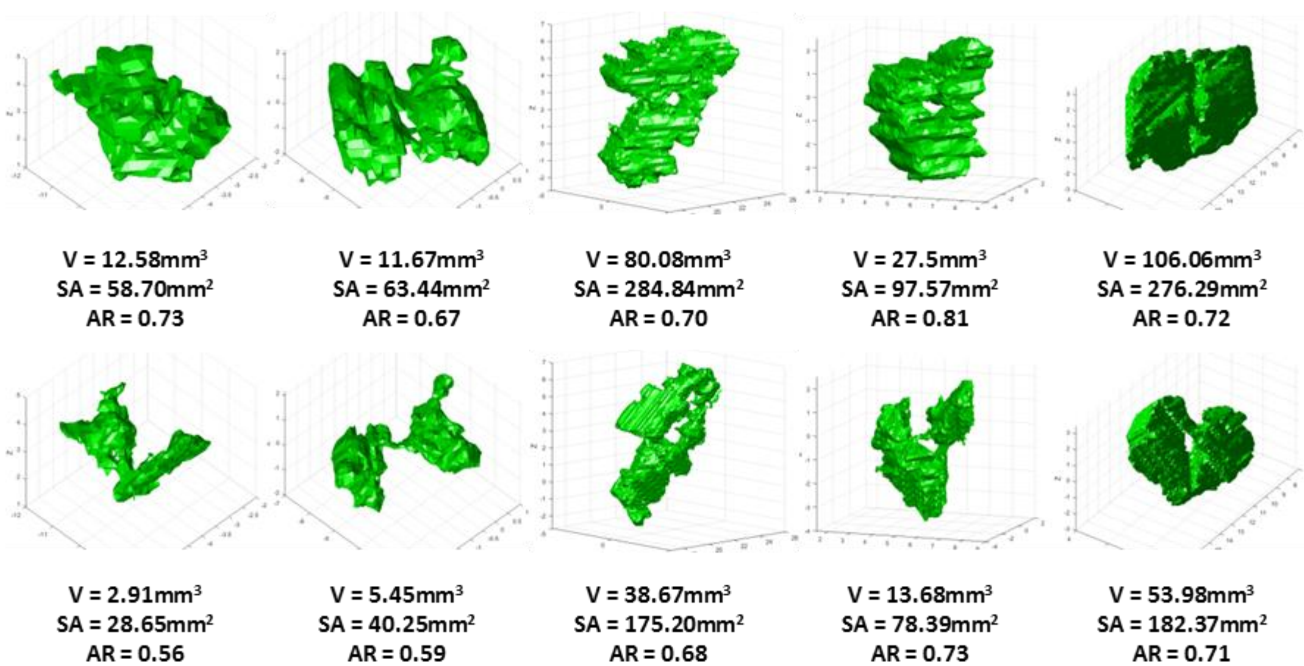

Figure 18. 3D reconstructions of five different recorded snowflakes based on three-camera (top panels) and five-camera (bottom panels) MASC instruments. For each reconstruction, the corresponding computed volume (V), surface area (SA), and aspect ratio (AR) are given as well. The unit of the grid is mm.

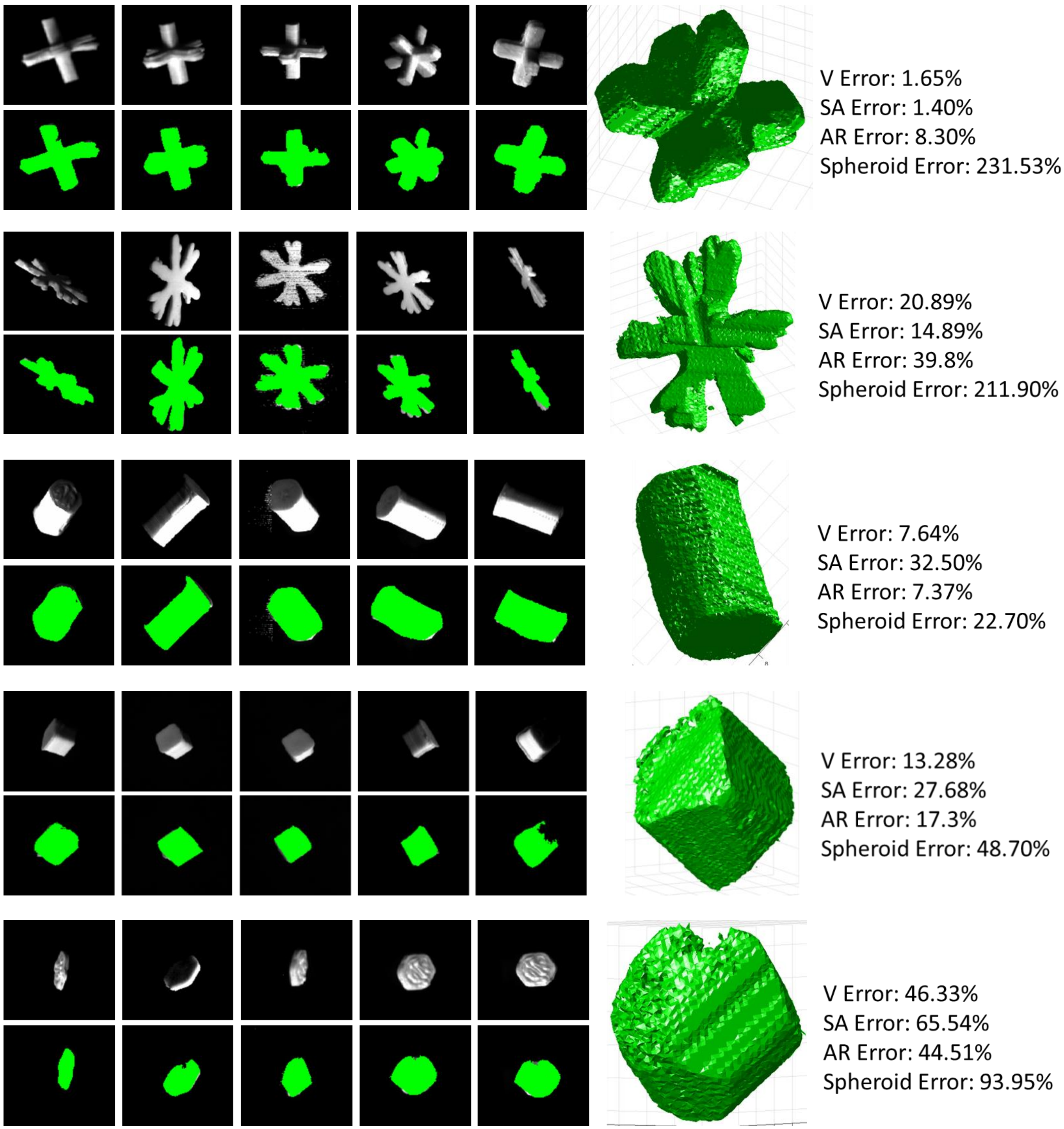
V Error: 1.65%
SA Error: 1.40%
AR Error: 8.30%
Spheroid Error: 231.53%
V Error: 20.89%
SA Error: 14.89%
AR Error: 39.8%
Spheroid Error: 211.90%
V Error: 7.64%
SA Error: 32.50%
AR Error: 7.37%
Spheroid Error: 22.70%
V Error: 13.28%
SA Error: 27.68%
AR Error: 17.3%
Spheroid Error: 48.70%
V Error: 46.33%
SA Error: 65.54%
AR Error: 44.51%
Spheroid Error: 93.95%

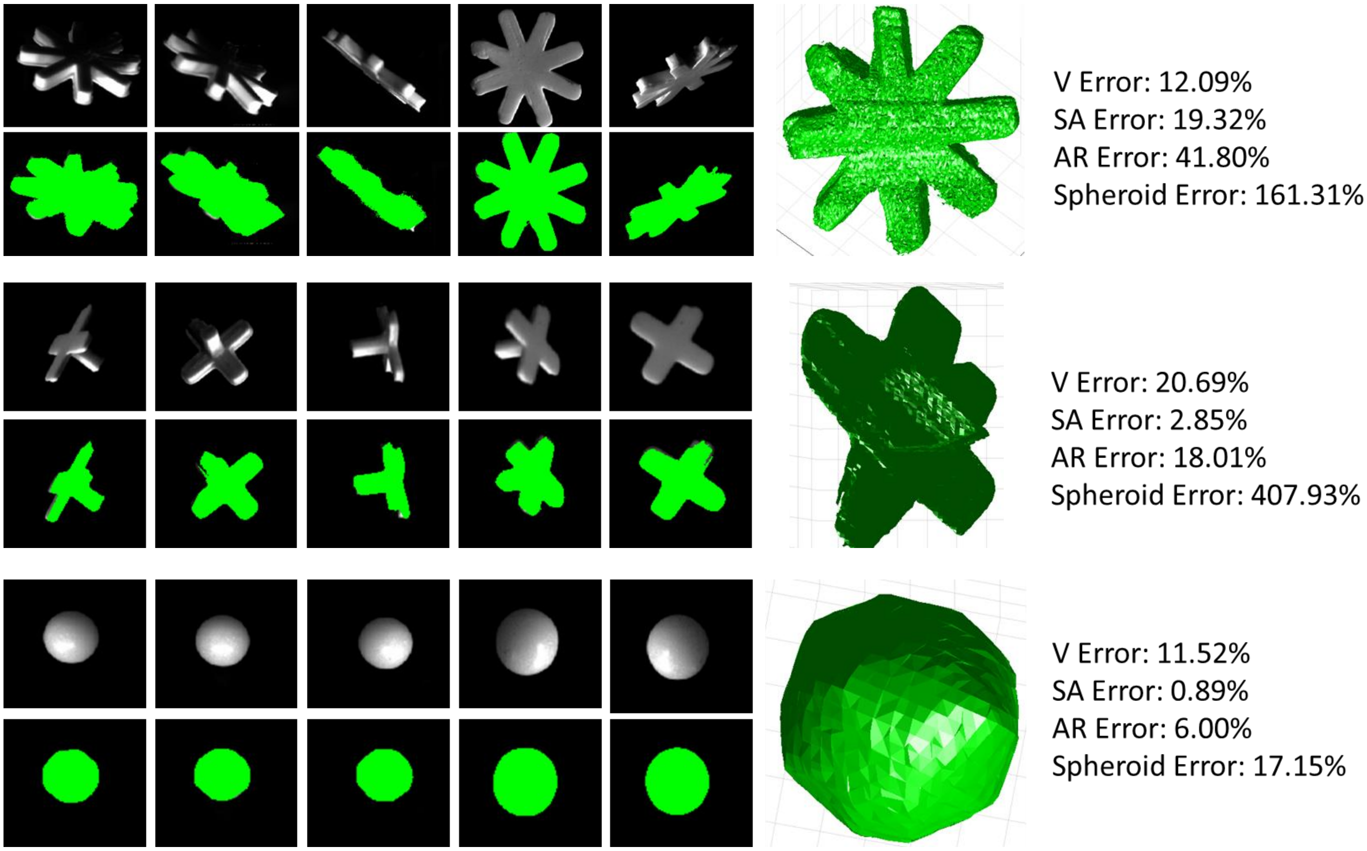

Figure 19. Visual hull reconstructions of 3D printed fake snowflakes and the corresponding MASC images, along with the projections of 3D reconstructed shapes onto 2D images. Percent errors of the volume (V), surface area (SA), and aspect ratio (AR) of the 3D reconstructions relative to the V, SA, and AR values of the 3D CAD models of 3D printed snowflakes are given as well. The volume percent error with respect to the V of the CAD models is shown also for the reconstructions of fake snowflakes using spheroids instead of the visual hull method.

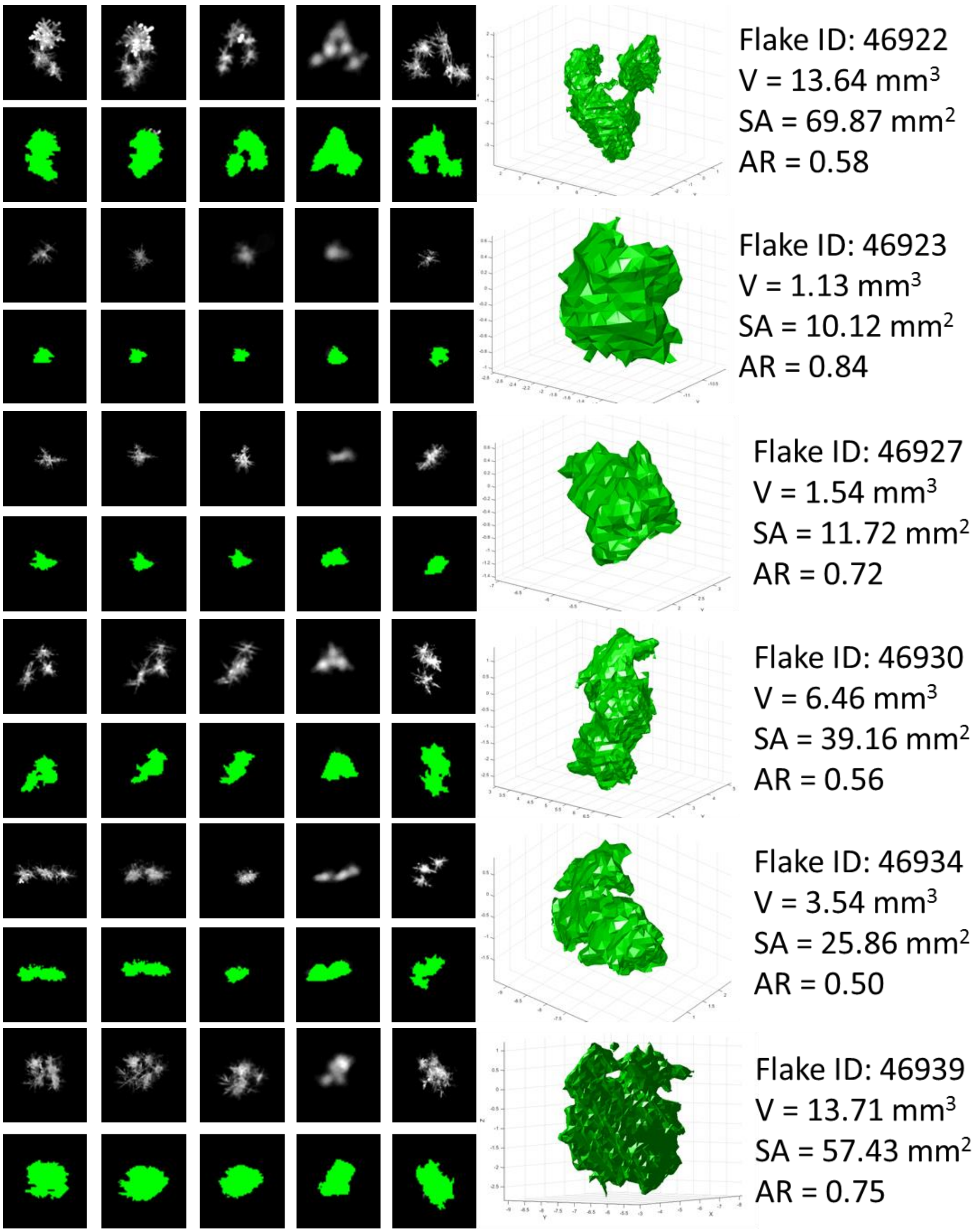
Flake ID: 46922
V = 13.64 mm³
SA = 69.87 mm²
AR = 0.58
Flake ID: 46923
V = 1.13 mm³
SA = 10.12 mm²
AR = 0.84
Flake ID: 46927
V = 1.54 mm³
SA = 11.72 mm²
AR = 0.72
Flake ID: 46930
V = 6.46 mm³
SA = 39.16 mm²
AR = 0.56
Flake ID: 46934
V = 3.54 mm³
SA = 25.86 mm²
AR = 0.50
Flake ID: 46939
V = 13.71 mm³
SA = 57.43 mm²
AR = 0.75

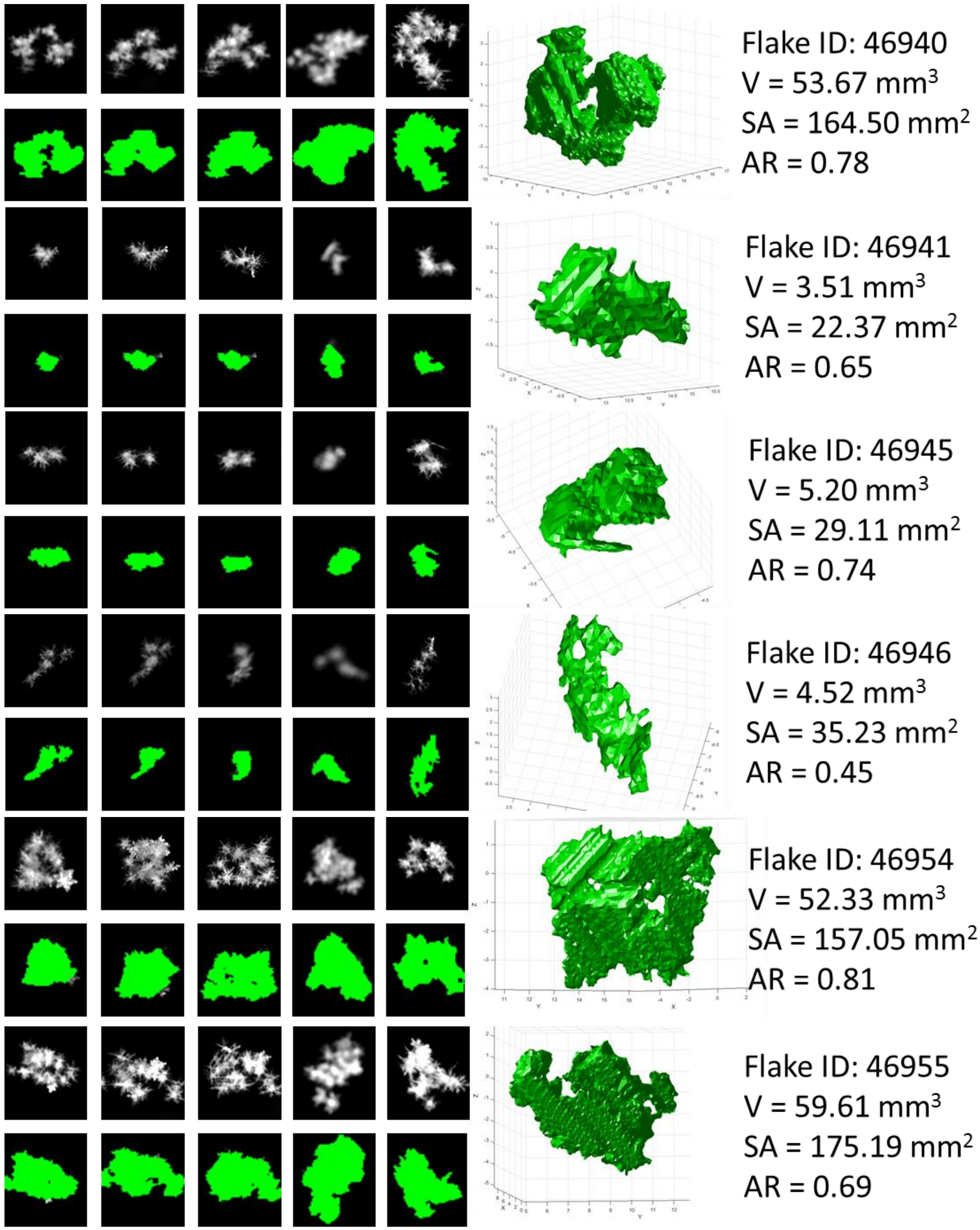
Flake ID: 46940
V = 53.67 mm3
SA = 164.50 mm2
AR = 0.78
Flake ID: 46941
V = 3.51 mm3
SA = 22.37 mm2
AR = 0.65
Flake ID: 46945
V = 5.20 mm3
SA = 29.11 mm2
AR = 0.74
Flake ID: 46946
V = 4.52 mm3
SA = 35.23 mm2
AR = 0.45
Flake ID: 46954
V = 52.33 mm3
SA = 157.05 mm2
AR = 0.81
Flake ID: 46955
V = 59.61 mm3
SA = 175.19 mm2
AR = 0.69

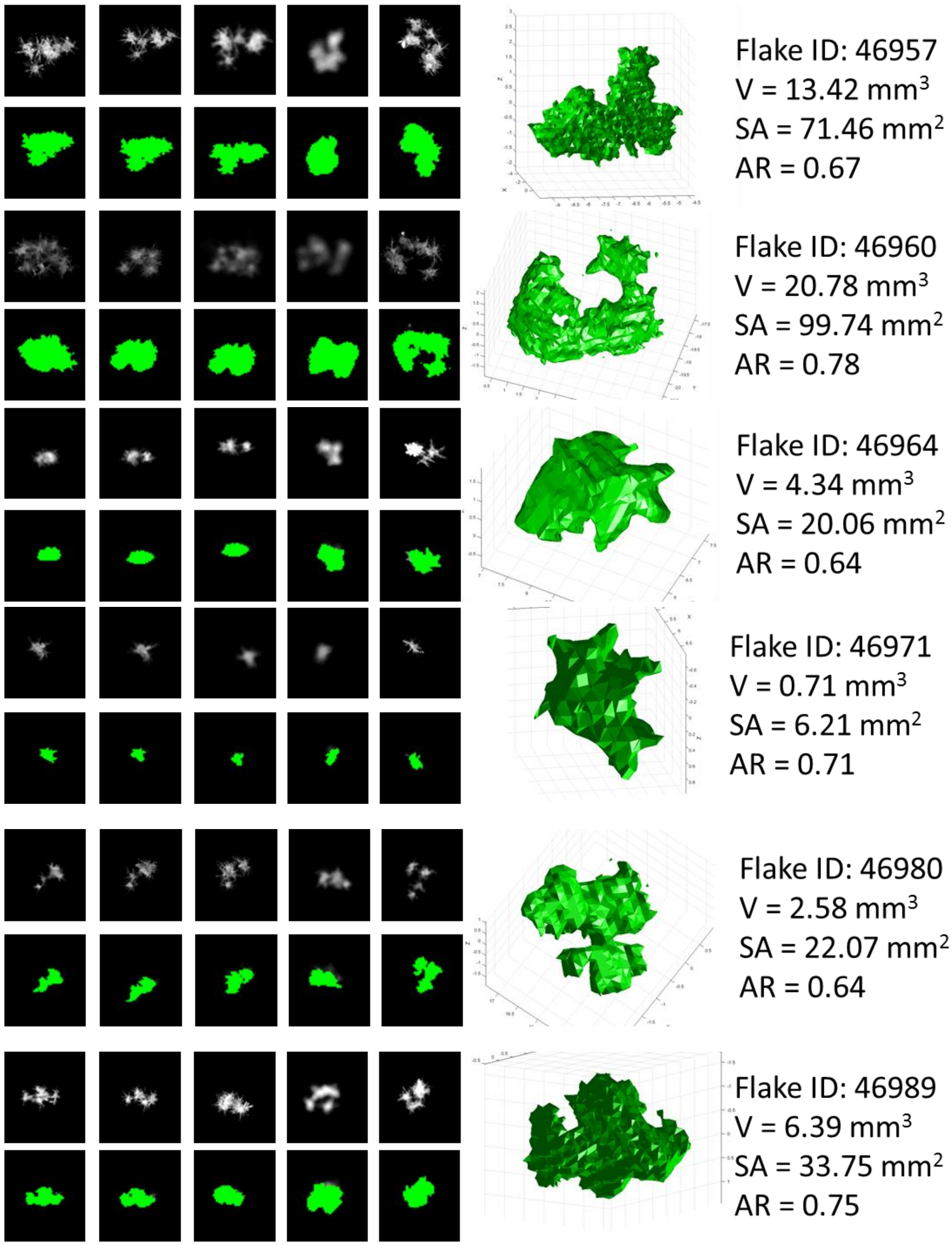
Flake ID: 46957
V = 13.42 mm^3
SA = 71.46 mm^2
AR = 0.67
Flake ID: 46960
V = 20.78 mm^3
SA = 99.74 mm^2
AR = 0.78
Flake ID: 46964
V = 4.34 mm^3
SA = 20.06 mm^2
AR = 0.64
Flake ID: 46971
V = 0.71 mm^3
SA = 6.21 mm^2
AR = 0.71
Flake ID: 46980
V = 2.58 mm^3
SA = 22.07 mm^2
AR = 0.64
Flake ID: 46989
V = 6.39 mm^3
SA = 33.75 mm^2
AR = 0.75

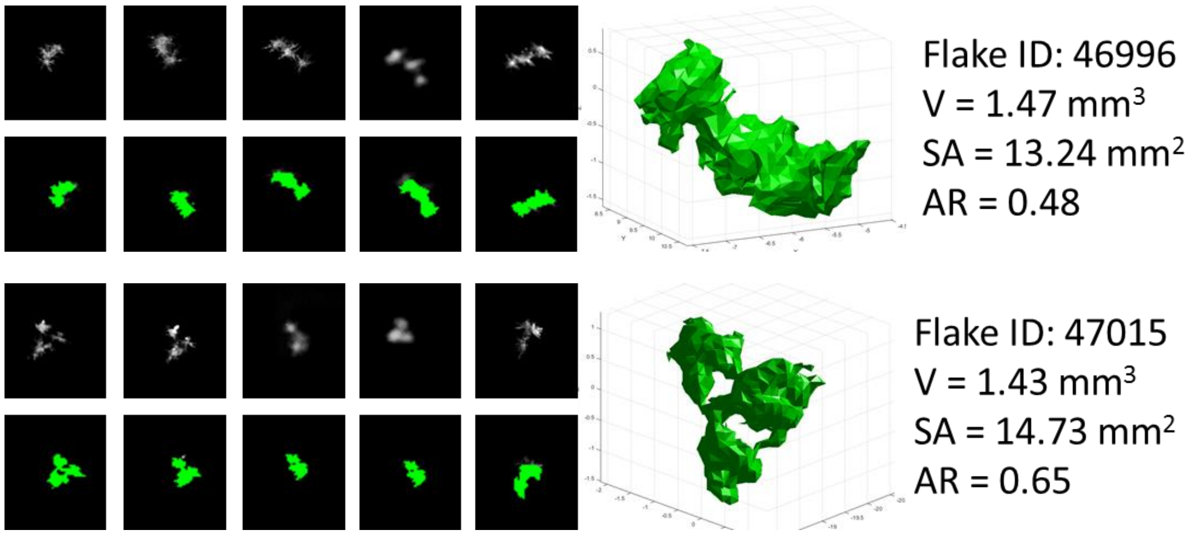

Figure 20. 20 examples of 3D visual hull reconstructions of different snowflakes collected at the MASCRAD Field Site (Fig. 1) during a February 23rd, 2015 snow event. For each snowflake, the five photographs from the modified MASC system (Fig. 2) are shown along with the 3D reconstructed shape triangular mesh and its back projections onto the original images. To the right of each 3D reconstruction, the calculated volume (V), surface area (SA), and aspect ratio (AR) of the mesh are given as well. The unit of the grid is mm.